

Probing forced responses and causal mechanisms in large-scale climate dynamics with reduced-order neural models

Fabrizio Falasca*

*Courant Institute of Mathematical Sciences
New York University, New York, NY, USA*

(Dated: October 9, 2025)

A central challenge in climate science and applied mathematics is developing data-driven models of multiscale systems that capture not only stationary statistics but also responses to external perturbations. Current neural climate emulators seek to resolve the atmosphere–ocean system in all its complexity but often fail to reproduce forced responses, limiting their use in causal studies such as Green’s function experiments. Response theory offers a rigorous framework to explore these limitations, moving beyond stationary statistics, probing causal mechanisms, and guiding model design. Using a simplified multiscale system, we argue that the skill of purely data-driven models in reproducing perturbed statistics depends critically on (i) identifying the proper variables to model, including spatial and temporal scales, and (ii) accurate stochastic parameterizations of unresolved processes. For studies of low-frequency climate dynamics, these insights motivate reduced-order neural models, tailored to *specific* processes, as valuable alternatives to *general-purpose* emulators. We illustrate this perspective with a reduced-order neural stochastic model designed to investigate responses of radiative fluxes to surface temperature perturbations. The model largely reproduces stationary statistics and enables the study of forced responses in both ensemble mean and variance, shifting the study of climate feedbacks from single trajectories to responses of probability distributions. These results underscore reduced-order models, augmented with modern neural networks and evaluated within the framework of response theory, as a practical strategy for causal inference and attribution studies in large-scale climate dynamics.

I. INTRODUCTION

A key challenge in current applied mathematics is to build data-driven models from partial observations of multiscale physical systems. Among the most challenging examples is the climate system: a forced, dissipative, and chaotic system whose dynamics span at least 15 orders of magnitude across spatial and temporal scales [1]. This problem has been extensively studied over the past three decades, mainly in the realm of reduced-order models [2]. Seminal contributions include the work of Penland and collaborators [3–5], the multilevel modeling strategies of Kravtsov and colleagues [6–9], and the contributions of Majda et al. [10, 11]. Recent proposals include Markov-chain models as in [12–14] and novel ideas from generative models [15]. Most prior work has focused on evaluating reduced-order models on equilibrium statistics and forecasting, with limited attention to responses to *external* perturbations, an exception being the contributions of Majda and collaborators (see e.g. [16]). Capturing such responses is key for building models that not only mimic the system’s dynamics but also faithfully capture causal relations across degrees of freedom [17, 18].

Recently, autoregressive models based on deep learning architectures have been proposed as potential *emulators* of complex turbulent systems such as the weather [19–23] and climate [24–33] systems. Unlike traditional

reduced-order models, these neural architectures aim to emulate the full hierarchy of spatial and temporal scales present in the system. For example, [30] and [31] emulate the full ocean and atmosphere components of state-of-the-art climate models. Such emulators often reproduce stationary statistics and generate forecasts across a range of horizons, offering a promising direction for efficient climate modeling. However, several limitations remain. Long rollouts suffer from error accumulation that can drive instabilities [34, 35]. Moreover, current emulators are unable to capture extreme events if not already present in the training set, preventing their use for rare-event analysis in a changing climate [36]. More relevant here, skill in reproducing stationary statistics does not guarantee accurate responses in perturbation experiments, restricting their use for causal studies of climate dynamics. This has two consequences: (i) neural emulators often fail to generalize in out-of-distribution climate change scenarios, and (ii) they may not capture the correct causal relations across variables, two issues that are likely related. The work of Van Loon et al. [37] illustrates this limitation in the context of the “pattern effect” problem [38, 39], i.e. the influence of sea surface temperature (SST) warming patterns on Earth’s energy imbalance. Using the ACE2 emulator [26] trained on ERA5 [40], they constructed a Green’s function by perturbing SSTs regionally and measuring the radiative response. The resulting Green’s function failed to capture the causal relation between SST and radiative fluxes in a quantitative way. This is just one example of limitations of neural emulators in capturing responses to perturbations with additional examples in

* fabri.falasca@nyu.edu

[30, 31, 41]. Even if such issues are addressed in specific cases, see [42] in the context of the pattern effect, they highlight a broader challenge: building general-purpose emulators that reliably capture forced responses remains inherently difficult and context-dependent. Moreover, most current emulators represent only a subsystem (e.g., atmosphere or ocean), and limitations in responding to perturbations are expected to worsen in coupled models. Overall, limitations in capturing forced responses suggest that neural emulators are not yet ready for causal applications in climate dynamics.

While the field of neural emulation is advancing rapidly, it is useful to step back and examine its fundamental limitations in capturing forced responses, both from a theoretical standpoint and in controlled settings. In the first part of this paper, we build on a series of previous works by A. Vulpiani and collaborators on the limitations of data-driven modeling [43–45]. We consider a simplified stochastic dynamical system and ask the following question: *Can neural autoregressive models, trained on (practically) infinitely long time series, accurately capture the response to general external perturbations?* In addressing this question, we focus on two relevant scenarios in data-driven-only modeling:

- *Unknown equations, fully observed state vector.* Data-driven modeling when the entire state vector is available. Here, we assume no knowledge of the underlying equations, but we have access to very long time series of the complete system state vector.
- *Unknown equations, partially observed state vector.* Data-driven modeling in the presence of partial observations. This reflects common constraints in modeling high-dimensional systems from data, where the full set of relevant variables is typically unknown. In this more realistic setting, we again assume no knowledge of the underlying equations and only partial access to the system’s state vector.

To tackle such questions we proceed pedagogically by focusing on a multiscale “triad model” first proposed by Majda and collaborators in [46, 47]. The model mimics the abstract structure of dynamical cores in large-scale climate models with a linear operator and an energy conserving nonlinear, quadratic operator. It provides a simplified yet relevant mathematical framework to unambiguously explore key limitations in capturing forced responses in climate emulators. We address the questions above by training neural stochastic emulators on a long integration of the triad model and test the models’ performance on stationary and perturbed cases. In doing so, we face the following issue: quantifying how an emulator respond to general forcing is an ill-posed question, as there are infinite possible forcings. Nonetheless, the linear response to a general forcing can be computed by convolving the forcing with an impulse response operator [48, 49]. This operator can be inferred

from the model and is a *building block* that an emulator must capture to reproduce the response to small, general external perturbations [48], as well as the cause-effect relations among variables [17]. In the case of a fully observed state vector we show that the inferred neural model can reproduce stationary and perturbed statistics of the system. In the case of partial observations, as in realistic settings, the performance of a data-driven model necessarily depends on (i) the choice of proper variables to model and (ii) suitable parameterizations of unobserved processes. The field of reduced order modeling, introduced earlier, has long sought to confront these challenges by formulating effective Langevin equations capturing the coarse-grained, slow dynamics of the system [5, 50, 51], though typically without addressing responses to external perturbations. Therefore, we will argue that, in the case of low-frequency climate dynamics, a promising perspective is to build on such established approaches, emphasizing coarse-grained dynamics and stochastic parameterizations, while using neural networks as powerful tools within this framework.

We emphasize that the focus on a simplified dynamical system is not a limitation in this context. In fact, the goal is not to demonstrate the success of a method, but to illustrate, by analogy, fundamental issues of data-driven modeling that are already evident in low dimensions and are likely to become more pronounced in higher-dimensional settings. As Smith (2002) [52] argues, while it is unreasonable to expect solutions to low-dimensional problems to generalize to high dimensions, so too it is unlikely that limitations observed in low-dimensional systems will vanish in high-dimensional, operational models. The first part of this paper is pedagogical in nature, aiming to bridge perspectives across researchers in statistical physics, climate science, and machine learning, while also providing practical methodological tools for the design and evaluation of data-driven models.

Building on these ideas, we conclude this study by considering a real-world example. Throughout this paper, we emphasize, when possible, the distinction between “real-world examples/systems” and merely high-dimensional dynamics. By real-world examples we refer to situations where (i) we observe only the temporal evolution of a subset of variables without access to the full state vector (i.e. a projection of the full dynamics) or (ii) where even in the presence of all variables the system encompasses a huge number of spatial and temporal scales. Both cases (i) and (ii) lead to the need to formulate *effective* rather than *primitive* equations for both practical and conceptual reasons [50]. For an early instance of case (ii), see the work of Charney (1948) [53], Charney et al. (1950) [54] and the discussion in Dalmedico (2001) [51]. The example we consider is the “pattern effect” introduced above, which requires Green’s function experiments to quantify the response of top-of-atmosphere (TOA) radiative fluxes to

perturbations in the sea surface temperature (SST) field. To this end, we develop a simplified stochastic neural model that emphasizes a large-scale representation of SST and global-mean net radiative flux, rather than attempting to resolve all spatial and temporal scales of variability as in current emulators. We discuss the coarse-graining and preprocessing choices relevant for model construction. The model largely reproduces both stationary and forced statistics and, importantly, enables Green’s function–like experiments to infer direct causal relations between SST and TOA radiative flux, a task where general-purpose emulators can perform poorly [37]. Crucially, we focus on responses in the ensemble mean and variance, rather than single trajectories as in most current studies, thereby extending the concept of climate feedback to include changes in distributional properties.

The paper is organized as follows: in Section II we introduce the theoretical ideas underpinning this work. In Section III we discuss key conceptual difficulties in data-driven modeling of real-world dynamical systems. In Section IV we present a real-world application by focusing on radiative feedbacks to temperature perturbations. Conclusions then follow in Section V.

II. THEORETICAL FRAMEWORK: DATA-DRIVEN STOCHASTIC CLIMATE MODELING AND RESPONSE THEORY

We begin by outlining the main theoretical concepts that underpin this work. First, we briefly introduce general ideas for reduced-order stochastic modeling relevant for climate dynamics. We then review key aspects of response theory, which offers a rigorous framework to move beyond the evaluation of stationary dynamics, probe causal mechanisms, and ultimately guide model design.

A. Reduced-order stochastic climate models: theoretical and practical considerations

A general dynamical system can be represented in the form

$$d\mathbf{u}/dt = \mathbf{F} + \mathbf{L}\mathbf{u} + \mathbf{n}(\mathbf{u}), \quad (1)$$

where \mathbf{F} , \mathbf{L} and $\mathbf{n}(\mathbf{u})$ represent an external forcing, a linear and nonlinear operators, respectively. \mathbf{u} is not necessarily finite dimensional, and in the context of coupled atmosphere-ocean variability, it could in principle represent the deviation of all fields, at all scales, from their climatology [4]. However, for obvious practical reasons, Eq. (1) needs to be simulated on finite spatial and temporal resolutions. In contrast to numerical weather prediction, which demands high spatial and temporal resolution, low-frequency climate variability is governed by

a few dominant large-scale modes [4, 7, 18, 47, 48, 55]. The goal of reduced-order stochastic climate models is to develop low-dimensional models simulating large-scale, coarse-grained climate dynamics. The cumulative effect of unresolved fast variables, present at smaller spatial scales, is parametrized as stochastic terms. More formally, we decompose \mathbf{u} into slow and fast components, $\mathbf{u} = (\mathbf{x}, \mathbf{y})$, leading to an *effective* Langevin equation of the form:

$$d\mathbf{x} = \mathbf{f}_{eff}(\mathbf{x})dt + \mathbf{\Sigma}(\mathbf{x})d\mathbf{W}, \quad (2)$$

where \mathbf{f}_{eff} represents the deterministic “drift” dynamics, \mathbf{x} are the slow variables and \mathbf{W} is the standard Wiener process. The noise covariance matrix $\mathbf{\Sigma}$ can be independent of \mathbf{x} , corresponding to additive noise, or state-dependent $\mathbf{\Sigma}(\mathbf{x})$ corresponding to multiplicative noise. In the latter case, the equation is here interpreted in the Itô sense. Equation (2) is mathematically justified in the limit of infinite time-scale separation between fast and slow modes [1]. In the most general (and often intractable) setting, the effective dynamics of the slow variables also involve memory effects induced by the fast degrees of freedom, leading to non-Markovian dynamics. Kondrashov et al. (2015) [7] addressed this problem in a practical and efficient way by introducing the framework of multilevel stochastic models. Nonetheless, appropriate coarse-graining procedures have been shown to effectively average out non-Markovian contributions in many climate applications, yielding useful Markovian approximations [3, 4]. We refer the reader to [2] for a review on the role of non-Markovian contributions in effective climate equations and to [56, 57] for specific examples.

Reduced-order stochastic climate models, as in Eq. (2), provide an efficient alternative to state-of-the-art climate models for studying low-frequency climate variability. They are much more computationally efficient and allow us for mechanistic understanding of climate dynamics by isolating core processes and examining their qualitative behavior. This has fueled the development of low-dimensional stochastic models learned either from data [2–4, 7, 10, 16, 58, 59] or from known equations [46, 60–63], as well as inference-based techniques to infer interactions across modes of variability [18, 64–66].

In practice, given a phenomenon of interest, we typically begin with spatiotemporal data consisting of N time series of length T . We then often proceed as follows:

Coarse-grained dynamics. In spatiotemporal dynamical systems like climate, coarse-graining involves: (i) choosing a limited set of climate fields (e.g. temperature, velocities etc.), (ii) retaining a few relevant modes or large-scale averages, (iii) restricting the range of temporal scales. Throughout the paper, we will often refer to the so-called *proper* variables as the coarse-grained spatiotemporal fields obtained via (i–iii). The

relevant modes are often identified through Empirical Orthogonal Functions (EOFs) [8, 67], by retaining the first $n < N$ of such bases. The correspondent principal components (PCs), serve as the reduced time series for model training. Although EOFs are convenient, they may not be always optimal, and alternatives such as in [18, 68, 69] may be more suitable depending on the application. The performance of the final model is sensitive to all coarse-graining choices (i–iii); see, e.g., [70, 71]. Identifying the “right” coarse-grained representation remains one of the hardest challenges in data-driven modeling, as no general mathematical principle exists to guide such choices in high-dimensional dynamical systems [17, 43].

Inferring a stochastic model. Given the coarse-grained data \mathbf{x} , the goal is to infer a stochastic Markovian model as in Eq. (2). We summarize several traditional approaches that motivate our work, while acknowledging that many other methods exist beyond those discussed here. The simplest example is the Linear Inverse Model (LIM) proposed by Penland [3], where the drift is linear and the noise is additive, both estimated directly from data. LIMs have shown forecasting skill for sea surface temperature anomalies comparable to climate models [4, 5, 72, 73], and extensions exist to handle colored noise [74]. Kravtsov et al. (2005) and Kondrashov et al. (2015) [6, 7] generalized this framework through multilevel regression, incorporating quadratic drift terms and non-Markovian effects. These models perform well for stationary statistics [8] and forecasting [75]. The work of Majda and Harlim extended the multilevel regression framework by proposing stability constraints [11]. A theoretically grounded alternative is the approach of Majda, Timofeyev, and Vanden-Eijnden [60–63], dubbed MTV by the authors, which derives effective equations for the coarse-grained variables \mathbf{x} rather than assuming them. MTV has been successful for simplified models, though less so for complex climate systems, likely due to choices of coarse-graining steps (i–iii) shown above rather than intrinsic limitations, see also discussion in [8]. We will expand on this approach in Section III and Appendix B.

Overall, these works demonstrated that robust reduced-order stochastic climate models can be built through relatively simple regression strategies. In this paper, we build on these insights and investigate how simple neural architectures can infer both the drift and state-dependent noise in Eq. (2), with minimal assumptions. Our neural models retain a decomposition into linear and nonlinear terms, \mathbf{L} and $\mathbf{n}(\mathbf{x})$, as in the general representation of dynamical systems in Eq. (1). Furthermore, we will propose simple solutions to fit multiplicative (state-dependent) noise in high dimensions.

B. Response theory: a (very) brief overview

In this paper, we argue that data-driven models should be tested on their ability to capture both stationary statistics and responses to external perturbations. Assessing responses to arbitrary forcings is ill-posed, as the space of possible perturbations is essentially infinite. A way forward is to consider small impulse perturbations, which allow us to define a response operator and derive general conclusions about causality and forced responses within the linear response regime.

a. Impulse response operator. Given a n -dimensional coarse-grained state vector $\mathbf{x}(t) = [x_1, x_2, \dots, x_n](t)$, we perturb a degree of freedom x_j with a small, step function perturbation $x_j(0) \rightarrow x_j(0) + \delta x_j(t)$, with $\delta x_j(t) = \Delta_j \delta(t)$, where $\delta(t)$ is a delta function and Δ_j is a small perturbation amplitude [17, 76]. We then consider a general observable $A(x_k(t))$ (i.e. a general functional of the system) and quantify its response, in terms of ensemble average, as:

$$\delta \langle A(x_k(t)) \rangle = \langle A(x_k(t)) \rangle_p - \langle A(x_k(t)) \rangle, \quad (3)$$

where $\langle \cdot \rangle$ refers to ensemble average and the subscript “p” refers to the perturbed system. In this paper we are going to focus on two different specific observables: (i) $A(x_k(t)) = x_k(t)$ and (ii) $A(x_k(t)) = (x_k(t) - \mu_k(t))^2$, with $\mu(t)$ representing the time-dependent mean of the distribution. The two observables allow us to capture time-dependent responses in the mean and variance of the perturbed distribution respectively. The impulse response operator $\mathbf{R}(t) \in \mathbb{R}^{n,n}$ is then defined as:

$$R_{k,j}(t) = \lim_{\delta x_j(0) \rightarrow 0} \frac{\delta \langle A(x_k(t)) \rangle}{\delta x_j(0)}. \quad (4)$$

The utility of the inferred impulse response operator is two-fold:

- *Causal inference.* Understanding causal relations across degrees of freedoms in physical systems require us to study the effect of interventions on the system [77]. The inferred response operator quantifies time-dependent cause-effect dependencies across degrees of freedoms x_j and x_k [17, 18, 78–80]. We refer to Appendix A for details on the relation between the response operator and causality.
- *Response to generic time-dependent forcing.* The response operator $\mathbf{R}(t)$ can be used to predict the response of the system to small, but general, time-dependent external forcing $\mathbf{f}(t) \in \mathbb{R}^n$ applied directly to the system’s degrees of freedoms as:

$$\delta \langle A(x_k(t)) \rangle = \sum_j \int_0^t R_{k,j}(\tau) f_j(t - \tau) d\tau. \quad (5)$$

Importantly, while we assume linearity in the system's response, the formulas above are valid for both linear and nonlinear systems.

A data-driven model capable of accurately capturing the impulse response operator will also capture the time-dependent causal interactions across degrees of freedom. Response theory can then be used to assess the skills of emulators by going beyond purely statistical metrics such as r-squared, by for example assessing the causal sensitivity of the system to external perturbation [18]. Moreover, since the linear response to small perturbations is given by the convolution formula in Eq. (5), recovering the impulse response operator ensures a faithful approximation of the system's linear response to general forcings. For this reason, we view the impulse response operator as a fundamental *building block* that a data-driven model must reproduce to capture the response to small, general perturbations, and is necessary (but not sufficient) to capture nonlinear responses as well. Importantly, the response operator can be inferred from data alone through the Fluctuation-Dissipation Theorem [49], this is discussed in Appendix A.

III. LIMITATIONS OF DATA-DRIVEN MODELING BY ANALOGY: THE CASE OF PARTIAL OBSERVATIONS

A fundamental limitation of purely data-driven modeling of multiscale climate systems is that we cannot observe all degrees of freedom. Even when governing equations are known, as in meteorology, climate fields are only available at finite temporal and spatial resolution. Dynamics at smaller and faster scales are therefore missing from the data and often remain unparameterized in emulators, unlike in full climate models. An even greater challenge arises in many areas where we lack governing equations altogether to guide emulator construction. In both cases, data-driven approaches can mimic the observed variability of the retained variables, reproducing probability distributions, autocorrelation functions, and providing reasonable forecasts. Yet testing responses to perturbations, where unobserved dynamics becomes relevant, often exposes structural deficiencies that are otherwise hidden. The goal of this section is to illustrate such limitations within a controlled mathematical setting, where they can be made explicit and unambiguous.

A. A triad model as a simplified prototype for coarse-grained, stochastic climate modeling

We focus on a simplified yet relevant dynamical system that retains essential features of high-dimensional geophysical flows, making the conclusions of the Section meaningful for climate applications. The model was introduced by Majda and collaborators [46] and later used

in [47] in the context of climate dynamics. In what follows, we present the model and refer to Appendix B for an in-depth discussion on its relevance as a building block for complex turbulent flows. The triad model considered in this study takes the following form:

$$\begin{aligned} dx_1 &= (L_{11}x_1 + L_{12}x_2 + L_{13}x_3 + Ix_1x_2)dt \\ dx_2 &= (-L_{12}x_1 - Ix_1^2 - \gamma_2\epsilon^{-1}x_2)dt + \sigma_2\epsilon^{-1/2}dW_2 \\ dx_3 &= (-L_{13}x_1 - \gamma_3\epsilon^{-1}x_3)dt + \sigma_3\epsilon^{-1/2}dW_3 \end{aligned} \quad (6)$$

This idealized system mimics the functional structure of turbulent geophysical flows, featuring linear couplings L_{11}, L_{12}, L_{13} and energy-conserving quadratic nonlinearities. The parameter I controls the strength of the nonlinearity: when $I = 0$, the model reduces to purely linear dynamics and Gaussian statistics. The quadratic interactions, here between x_1 and x_2 , typically arise when geophysical turbulent flows are expressed in terms of orthogonal bases such as EOFs [16]. The parameter ϵ sets the time-scale separation between the slow mode x_1 and the fast modes (x_2, x_3) , allowing exploration of multi-scale dynamics in a controlled setting. The terms W_2 and W_3 represent independent Wiener processes, introducing stochastic forcing into the second and third equations. The model generates unimodal distributions with relatively small, but significant, deviations from Gaussianity, which is a relevant feature in the study of low-frequency climate variability [81] and found in both general circulation models and observational data, see e.g. [82–84].

B. The case of unknown equations but a fully observed state vector

We consider the relatively simple case of a low-dimensional dynamical system with only one characteristic time scale (i.e. $\epsilon = 1$). The parameters chosen for this first test are: $L_{11} = -2$, $L_{12} = 1$, $L_{13} = 1$, $\gamma_2 = 0.6$, $\gamma_3 = 0.4$, $\sigma_2 = 1.2$, $\sigma_3 = 0.8$, $I = 1$, $\epsilon = 1$. We now integrate the system in (6) with an Euler–Maruyama scheme for a period of length $T = 10^7$ with time step $dt = 0.01$ (i.e. 10^5 Model Time Units). Given the system's decorrelation time scale (shown later), the resulting time series can be effectively treated as infinitely long. Given this long trajectory of the full state vector $\mathbf{x}(t) = [x_1, x_2, x_3](t)$, we learn data-driven models directly from the time series. We construct both linear and nonlinear stochastic models. We specify the functional forms of these models and assess their ability to reproduce both the stationary and perturbed statistics of the original triad system.

1. Functional form of the data-driven models considered

We consider two data-driven models. To keep the main text focused, we leave the technical details of the fitting

procedures, along with details of the neural networks, in Appendix C.

- *Linear model.* We consider the following linear model:

$$d\mathbf{x} = \mathbf{L}\mathbf{x}dt + \Sigma d\mathbf{W}, \quad (7)$$

\mathbf{L} is a linear operator, $\Sigma\Sigma^T$ is the noise covariance matrix and \mathbf{W} is the standard Wiener process.

- *Nonlinear model.* The nonlinear model takes the following form:

$$d\mathbf{x} = (\mathbf{L}\mathbf{x} + \mathbf{n}(\mathbf{x}))dt + \Sigma d\mathbf{W}. \quad (8)$$

\mathbf{L} is a linear operator and $\mathbf{n}(\mathbf{x})$ is parametrized by a Multilayer Perceptron (MLP). Crucially, the term $(\mathbf{L} + \mathbf{n}(\mathbf{x}))$ is fitted jointly. In what follows we are going to often refer to this model as “neural model” or “neural emulator”.

The two models above are trained on a long simulation of the triad system in Eq. (6).

Note that this is the only Section in this work where we compare linear and nonlinear autoregressive models. The linear method is considered for two reasons. First, we show that linear inverse modeling (LIM), as originally proposed in [3], serves as a strong baseline for neural autoregressive models, successfully capturing both the mean and variance of the system’s stationary distribution, the autocorrelation functions, and the ensemble mean response to external perturbations. Second, and consistent with theoretical expectations [47], we demonstrate that linear models are fundamentally limited in capturing changes in the full probability distribution: for instance, they cannot represent any response in the variance to external forcings. This limitation restricts their usefulness for studying forced changes in distributions beyond the mean.

2. Stationary statistics

We integrate the two data-driven models inferred from data and specified in Eq. (7) and (8) for $T = 10^7$, yielding time series of the same length as those obtained from the original triad system. We then compare the modeled and original probability density functions (PDFs) and autocorrelation functions (ACFs), as shown in Figure 1. The neural model described in Equation (8) successfully captures the stationary distributions of $x_1(t)$, $x_2(t)$ and $x_3(t)$. In particular, it outperforms the linear model by accurately reproducing the non-Gaussian features of x_1 . Both models also reproduce the autocorrelation functions well, as seen in the second row of Figure 1. In summary, the neural emulator defined in Equation (8) is capable of capturing both the PDF and autocorrelations of the full state vector $\mathbf{x}(t)$. At the same time, the linear model serves as a strong baseline for evaluating more sophisticated data-driven approaches.

3. Response of probability distributions to external perturbations

a. Impulse response functions. We now examine the impulse response of the original triad model (Equation (6)), the linear model (Equation (7)), and the nonlinear neural model (Equation (8)). Specifically, we analyze the time-dependent response of observables $A(x_k(t))$, with $k = 1, 2, 3$, to an impulse perturbation imposed on $x_1(0)$ at time $t = 0$. We choose as observables the mean and variance of the time-dependent perturbed distribution and refer to Appendix A for details on how to compute the response operator. The results, shown in Figure 2, reveal that the nonlinear neural model captures the mean response of the distribution quantitatively, while the linear model captures it only qualitatively. The most significant differences arise in the response of the variance: the linear model yields exactly zero variance response, clearly highlighting the limitations of linear dynamics [47]. In contrast, the neural model captures the variance response with relatively high fidelity. We therefore consider the neural model presented here as a skillful model both in terms of reproducing the stationary distribution as well as the response operator.

b. Responses to a specific logarithmic forcing. we now consider a more targeted test involving a specific, time-dependent forcing. We introduce a logarithmic forcing term to the right-hand side of the original and data-driven triad model. The forcing is applied only to x_1 and takes the form $(0.01\log(1+t), 0, 0)$ per time step. Each model is integrated for 2500 time steps (25 Model Time Units), and we compute the difference between the forced and unforced simulations in terms of ensemble mean and variance responses. Results are presented in Figure 3. The neural model (Eq. (8)) accurately reproduces the forced responses across all three components. The linear model (Eq. (7)) performs qualitatively well but exhibits significant deviations in the ensemble mean response of the second mode x_2 as shown in Figure 3(b). This is consistent with the earlier Section: the largest error in the linear model’s impulse response also occurred in x_2 (see Figure 2(b)). This supports the interpretation that accurately capturing the impulse response operator is critical for a model’s reliability in predicting responses to general, time-dependent forcings. As expected, the linear model is not able to capture the response in ensemble variance. The neural model shows skillful response, capturing the time-dependent changes in ensemble variance relatively well, with the largest error in x_2 . In general, considering that the changes in variance are very small, we conclude that the neural emulator is skillful in responding to the imposed logarithmic forcing.

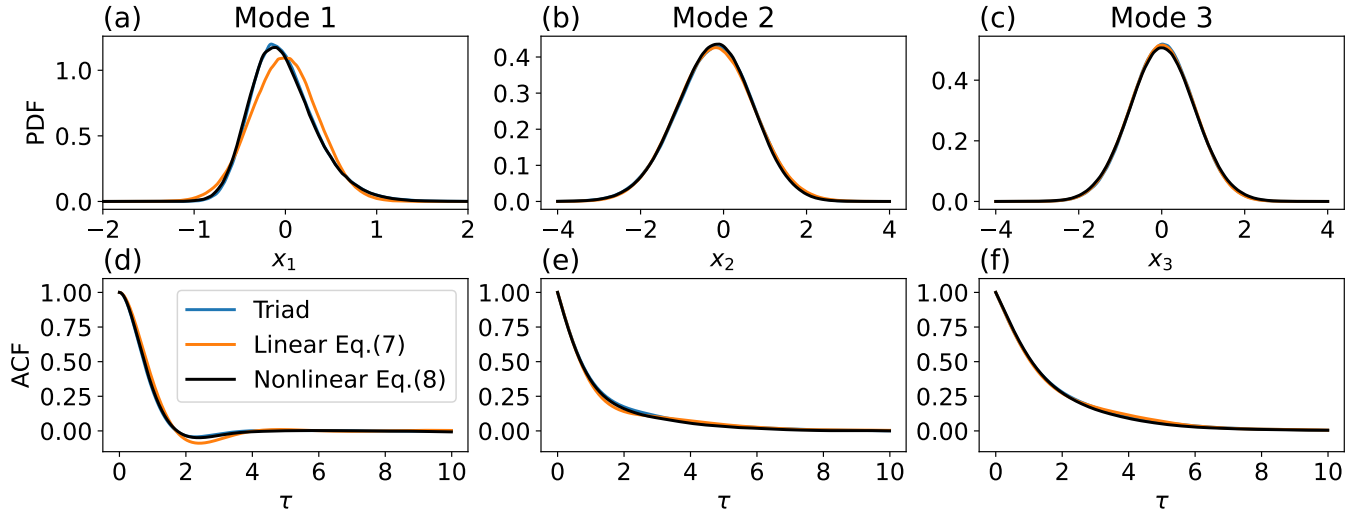


FIG. 1: First row: stationary distributions of the variables $x_1(t)$, $x_2(t)$ and $x_3(t)$ as modeled by the original triad system in Eq. (6), the linear emulator in Eq. (7) and the neural emulator in Eq. (8). Stationary distributions are obtained after running the three systems for 10^5 model time units. Second row: same as the first row but for the autocorrelation functions.

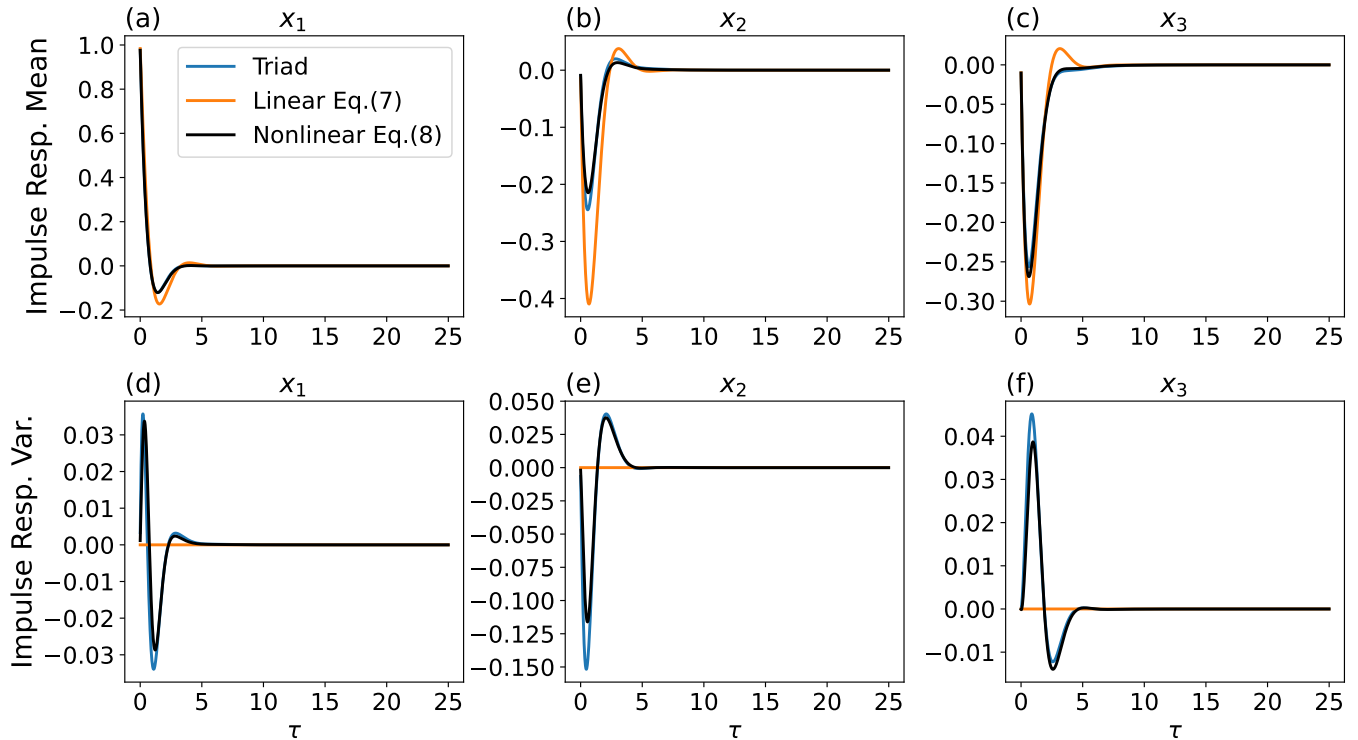


FIG. 2: Impulse response functions as modeled by the original triad system in Eq. (6), the linear emulator in Eq. (7) and the neural emulator in Eq. (8). First row: response of the ensemble mean to *impulse* perturbations imposed on $x_1(0)$ at time $t = 0$. Second row: response of the ensemble variance to *impulse* perturbations imposed on $x_1(0)$ at time $t = 0$. Impulse response functions are computed using an ensemble size of $N_e = 10^5$ members.

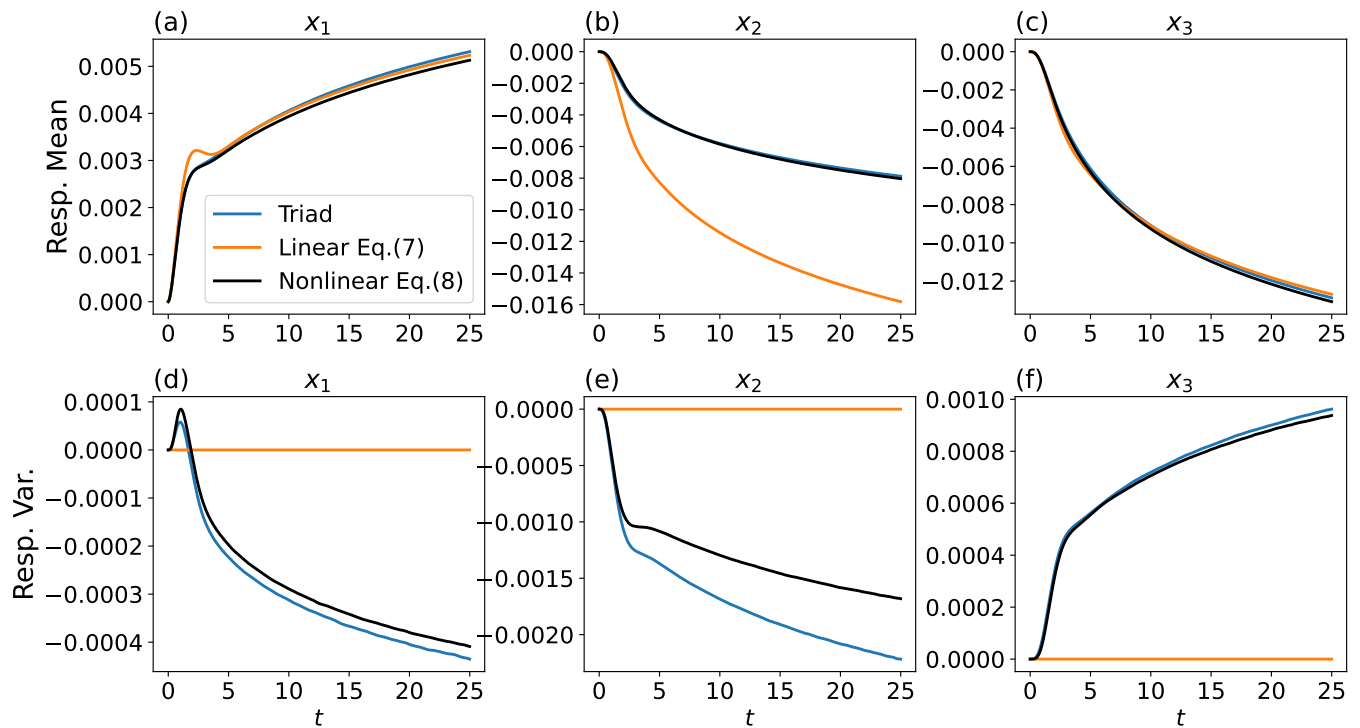


FIG. 3: Response to a small logarithmic forcing $F = (0.01 \log(1+t), 0, 0)$ imposed on the right-hand-side in Eq. (6), the linear emulator in Eq. (7) and the neural emulator in Eq. (8). First row: response of the ensemble mean to external forcing. Second row: response of the ensemble variance to external forcing. Responses are computed using an ensemble of $N_e = 10^5$ members.

4. Main takeaways

Given a (practically) infinitely long trajectory of a stochastic dynamical system, and assuming the ideal condition where the full state vector is observed, it is possible to construct a neural stochastic model that is stable, reproduces the stationary statistics, and responds accurately to small but general external perturbations. The analysis does not rule out that other systems may struggle to capture responses even with full observations; however, these issues are here regarded as technical rather than fundamental. Such technical issues can be addressed by considering more complex architectures or by adding constraints withing a chosen architecture. While these results are encouraging, they remain far from any real-world scenario. In practice, we typically have access only to partial observations of a complex, interconnected system.

C. The case of unknown equations and a partially observed state vector

We now return to the triad model defined in Eq. (6) and consider the more realistic scenario of model inference under partial observations and multiple timescales. The parameters chosen for this test are: $L_{11} = -2$,

$L_{12} = 0.2$, $L_{13} = 0.1$, $\gamma_2 = 0.6$, $\gamma_3 = 0.4$, $\sigma_2 = 1.2$, $\sigma_3 = 0.8$, $I = 1$, $\epsilon = 0.01$. In this setting the variable x_1 clearly is the slow mode, forcing the much faster modes x_2 and x_3 . We again integrate the system in (6) with an Euler-Maruyama scheme for a period of length $T = 10^7$ with time step $dt = 0.01$ (i.e. 10^5 Model Time Units).

Unlike the case considered in the previous section, where the entire state vector $\mathbf{x}(t) = [x_1, x_2, x_3](t)$ was available, we now consider a more challenging scenario: only one component of the system is observed (or available or chosen), either x_1 , x_2 , or x_3 . The modeling task is thus reduced to constructing a scalar stochastic model for the observed component alone. We require the scalar stochastic model to satisfy two criteria:

- i. It must reproduce the stationary statistics of the observed component;
- ii. It must correctly capture its response to perturbations as in the original triad system.

Criterion (ii) is particularly demanding because, in the triad model defined by Eq. (6), perturbations can propagate through the system, inducing cascades of feedbacks. These time-dependent feedbacks must be effectively parametrized within the scalar model, despite the absence of direct observations of some components.

While clearly nontrivial, this problem is representative of real-world data-driven modeling scenarios, where models are often built from partial observations of high-dimensional systems.

Proposing a scalar data-driven model from partial observations that satisfies the two criteria above raises two central challenges:

- *Choice of variable to model.* The reduced-order model depends critically on the choice of the modeled variable. Not all components can be selected to satisfy criteria (i) and (ii) discussed above. The only viable option is to model the slow mode x_1 , since the cumulative effect of the much faster x_2 and x_3 can be represented stochastically. Identifying such a *proper* variable is a necessary prerequisite for constructing a meaningful model under partial observations [43, 48, 85, 86]. In realistic spatiotemporal climate dynamics, this choice translates into selecting appropriate climate fields together with a narrow range of spatial and temporal scales as we will show in Section IV.
- *The need for suitable parametrizations.* Having identified the proper variable x_1 to model, the next challenge is to appropriately parametrize the cumulative effects of the unresolved components x_2 or x_3 onto the slow mode x_1 . This leads to the classic problem of stochastic parametrization [1, 2, 67, 87–89]. As we will show, the success of the resulting model, particularly in capturing forced responses, hinges critically on the quality of this parametrization.

We note that for the specific case of the triad model in Eq. (6), Majda and collaborators showed that an analytical reduced-order equation for the slow variable x_1 can be rigorously derived in the limit $\epsilon \rightarrow 0$ [46, 47]; see discussion in Appendix B. Our aim here is not to test such analytical strategies, which require full knowledge of the governing equations and are often limited in real-world settings; see footnote [90]. Rather, we use the triad model as a simple conceptual tool to highlight key challenges of data-driven modeling of multiscale systems. In realistic settings, both the governing equations and the full set of relevant variables are typically unknown [91]. Even before specifying a model structure, identifying the slow variables is nontrivial and highly problem-dependent.

In what follows, we assume that the proper slow variable, x_1 , has been correctly identified. Given this, we examine how the choice of stochastic parametrization and temporal coarse-graining influences the ability of neural models to emulate both stationary statistics and responses to perturbations. This discussion serves as a precursor to the more challenging real-world application in Section IV, where identifying the relevant variables requires a series of nontrivial coarse-graining decisions.

1. Functional form of the reduced order models considered

Given the correct choice of variable x_1 to model we now proceed in proposing two data-driven scalar models. Technical details of the fitting procedures are left to Appendix C. We consider two neural models:

- *Neural model with additive noise.* We consider the following neural model fitted using an artificial neural network, i.e. a Multilayer Perceptron (MLP). The model takes the following form:

$$dx = (Lx + n(x))dt + \sigma dW, \quad (9)$$

L is a linear operator (here just a scalar), $n(x)$ is a nonlinear operator and σ^2 is the noise variance. W is the standard Wiener process.

- *Neural model with multiplicative noise.* We consider a neural model as before, but now defined with multiplicative rather than additive noise:

$$dx = (Lx + n(x))dt + \sigma(x)dW. \quad (10)$$

The multiplicative (state dependent) noise $\sigma(x)$ is fitted with an additional neural network, see Appendix C.

To train the two models above we consider a long simulation of the triad system in Eq. (6) using the set of parameters reported in Section III C. We then extract only the time series of x_1 and train the models above on this long, scalar time series $x_1(t)$.

2. Stationary and perturbed statistics of the scalar model

We integrate the two data-driven scalar models in Eq. (9) and (10) for $T = 10^7$ time steps, yielding time series of the same length as the time series of $x_1(t)$ used for training. To evaluate the models' ability to capture both stationary and perturbed statistics, we examine the stationary probability distribution and the impulse response operator in ensemble mean and variance.

The neural model with additive noise (Figure 4(a)) fails to accurately capture the stationary statistics in a quantitative way. Moreover, the ensemble mean response to an impulse perturbation decays too slowly, and notably, the model fails to reproduce significant responses in the ensemble variance. In contrast, incorporating multiplicative noise (Eq. (10)) leads to a substantially improved representation of the stationary distribution, see Figure 4(e). The mean response remains largely unchanged, decaying too slowly, but the model now captures a qualitatively correct signal in the ensemble variance, albeit with a similarly slow decay.

These results indicate that the inclusion of multiplicative noise improves the reduced-order model's ability

to represent both stationary statistics and variance responses to perturbations. In the full triad system, perturbing x_1 at time $t = 0$ leads to changes in x_1 , x_2 and x_3 at the next time step dt . Consequently, x_2 and x_3 feedback on x_1 at the consequent time step. Such time-dependent feedbacks require the inclusion of state dependent noise $\sigma(x)$ to effectively parametrize such interactions. Moreover, as discussed in Appendix B, multiplicative noise is not an ad-hoc addition but is theoretically justified and explicitly predicted by rigorous mode reduction strategies [60]. However, even when multiplicative noise is considered, the responses to impulse perturbations are still only qualitatively right. We emphasize two key points:

- i. The analysis in Figure 4 highlights the importance of evaluating a model’s ability in predicting responses in higher-order moments, such as the variance. In the simple example discussed here, focusing solely on the ensemble mean response would lead to the incorrect conclusion that the two models respond to perturbations in the same way (see panels (b) and (e) in Figure 4).
- ii. Matching the stationary distribution quantitatively does not guarantee equally accurate responses to perturbations, as shown in Figure 4(d,e,f).

The presence of slowly decaying responses in the ensemble mean and variance to perturbations is indicative of a system that is no longer Markovian. The reduced-order stochastic scalar model is trained solely on the time series of $x_1(t)$. However, the time series $x_1(t)$ is generated by the full triad system in Eq. (6) and implicitly reflects the influence of the unobserved variables x_2 and x_3 on it. The variability of the unobserved variables x_2 and x_3 manifest as memory effects in the reduced order scalar model for x_1 . One strategy for addressing such memory effects is the multilevel regression approach first introduced by Kratsov, Kondrashov and Ghil (2005) [6] and later generalized by Kondrashov, Checkroun and Ghil (2015) [7]. The multilevel regression strategy augments the reduced-order model with a hierarchy of linear equations solving for the residuals from the deterministic dynamics and it can be thought as a practical implementation of the Mori–Zwanzig formalism in statistical mechanics [2, 7]. An alternative, pragmatic approach for handling non-Markovian effects is to coarse-grain the data in the temporal dimension, for instance, by averaging over a time window. This suppresses fast fluctuations within that window leading to an effective “Markovianization” of the dynamics. Due to its simplicity and practicality, this method is commonly used in the literature (see e.g. [4]) and is also adopted in the present study.

We therefore analyze the time series $x_1(t)$ from the long simulation of the triad system in Eq. (6). As an additional step, we average $x_1(t)$ over a short temporal

window of 10 time steps (equivalent to 0.1 Model Time Units). This averaging smooths out fast variability and effectively defines a coarse-grained system that is “more Markovian”. We then retrain the neural models with additive and multiplicative noise on the coarse-grained data. Results are shown in Figure 5. As before, the stochastic model with additive noise fails to capture the correct stationary and perturbed statistics. By contrast, the model with multiplicative noise not only reproduces the stationary distribution and improves the mean response, but also closely matches the variance response, capturing its peak magnitude and deviating only slightly in its temporal decay. One could, in principle, tune the averaging window to match the autocorrelation of the emulated $x(t)$ with that of the original $x_1(t)$, thereby ensuring closer agreement in the decay of responses (Figure 5(e,f)). We view this as a methodological refinement for future work, and leave it outside the scope of this study.

3. Main takeaways

Even with access to very long time series, modeling real-world dynamical systems from data alone remains fundamentally constrained by observing only a subset of the full state vector. This creates two major challenges: (i) the model’s skill depends critically on the variables chosen, and (ii) once these variables are fixed, the influence of unobserved degrees of freedom must be adequately parametrized. While such issues are illustrated with low-dimensional models, they become far more acute in realistic spatiotemporal climate systems, where time-scale separation is weak and variable selection involves nontrivial choices of fields, dimensionality reduction methods, and spatiotemporal scales. There is no rigorous mathematical framework to guide these choices from data alone.

Even in cases where the governing equations are known, such as in meteorology, and where large computational resources are available, emulators still operate on finite-resolution data, leading to subgrid processes. The cumulative effect of such unobserved processes still require parametrizations. This highlights that the problem of parameterizations, traditionally associated with numerical modeling [92, 93], is equally central to data-driven approaches with neural emulators.

These considerations highlight intrinsic limitations of general-purpose emulators in capturing responses to *external* perturbations and in supporting Green’s function-like experiments [38]. In contrast, reduced-order neural models are often tailored to specific problems, allowing one to leverage prior literature, insights, and results to guide variables and coarse-graining choices. In the next section, we present a concrete example where a simple reduced-order neural model succeeds in a task

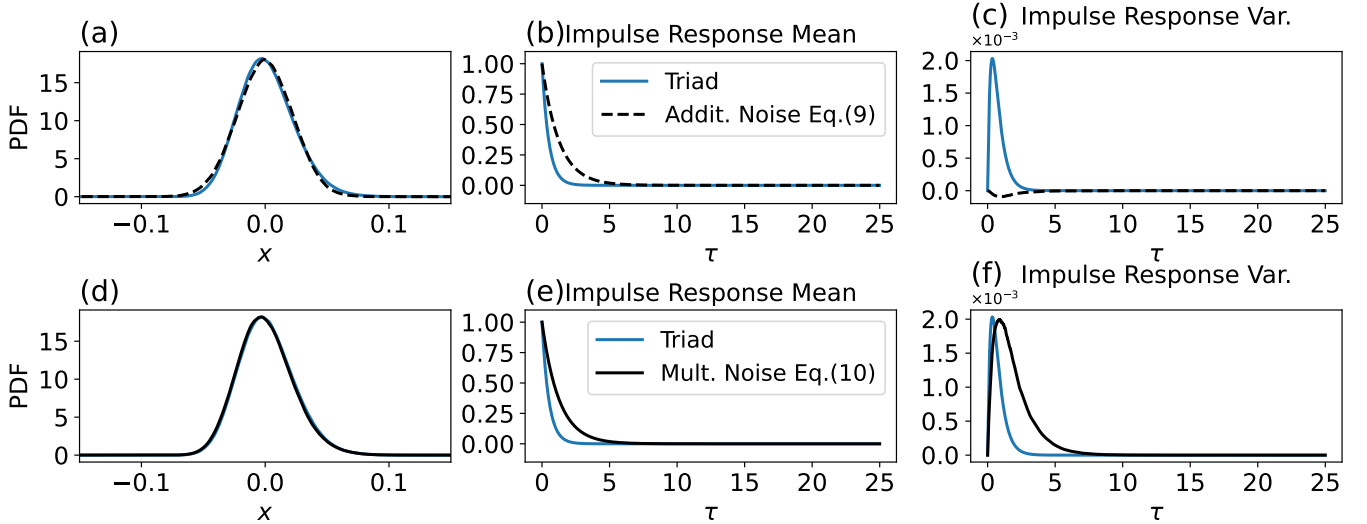


FIG. 4: First row: stationary probability distribution (panel (a)); ensemble mean response to an impulse perturbation (panel (b)); ensemble variance response to an impulse perturbation (panel (c)) for the variable x_1 in the triad system in Eq. (6) and the variable x in the neural scalar emulator with additive noise in Eq. (9). Second row: same as the first row but we are now considering the neural scalar emulator with multiplicative noise in Eq. (10). Impulse response functions are computed using an ensemble of $N_e = 10^6$ members.

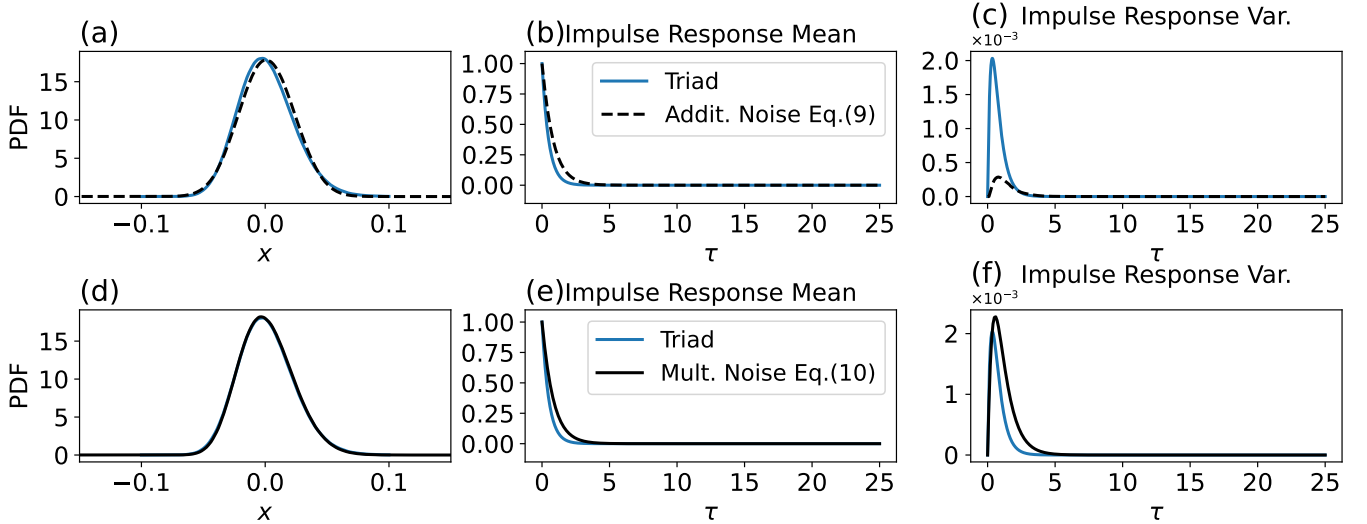


FIG. 5: Same as in Figure 4 however here the scalar emulators in Eq. (9) and Eq. (10) have been trained on a long trajectory of $x_1(t)$ after coarse-graining by averaging every 10 time-steps. No additional preprocessing was performed for the original triad system in Eq. (6), i.e. the blue curves in this Figure and in Figure (4) are the same.

where a state-of-the-art neural emulator showed limitations [37].

IV. A REAL-WORLD EXAMPLE: RADIATIVE RESPONSES TO TEMPERATURE PERTURBATIONS IN A CLIMATE MODEL

Building on the insights discussed above, we present a stochastic reduced-order model tailored to a specific real-

world test-case. We first introduce the scientific problem at hand and the form of the proposed emulator to tackle this specific question. We then highlight the coarse-graining choices defining the proper variables to model. Finally, we showcase the skill of this emulator to study causal mechanisms in large-scale climate dynamics.

A. Scientific problem at hand

a. The “pattern effect” problem. Radiative forcing (e.g., from changes in CO_2) drives surface warming, which alters sea surface temperatures (SSTs) and associated radiative feedbacks. Recent studies show that even for the same global-mean warming, different SST warming patterns can yield markedly different feedbacks. For example, eastern Pacific warming tends to amplify warming through positive feedbacks, while western Pacific (warm pool) warming has a stabilizing effect [38, 39]. This sensitivity of Earth’s energy imbalance to spatial SST patterns is known as the “pattern effect.” The pattern effect describes the fast response of top-of-atmosphere (TOA) radiative fluxes to spatial temperature variations and can be formalized in energy balance models via a Taylor expansion around the steady-state temperature [94].

A common approach to study the pattern effect is to relate SST patterns to TOA radiative fluxes using Green’s function experiments [95], where the radiative response to localized SST perturbations is quantified with atmosphere-only models [39, 96–99]. These experiments are valuable for testing model sensitivities but are computationally costly and typically require large SST perturbations (1–4 K) to obtain a measurable response within short simulations. Such large perturbations can trigger nonlinear behavior, undermining the linearity assumptions of the Green’s function framework [100]. This motivates the need for fast, interpretable data-driven models that can simulate responses of large ensembles at low cost and with small perturbation amplitudes. Furthermore, since climate models are known to be biased, data-driven emulators offer, in principle, a complementary way to learn climate dynamics directly from observations.

b. Possible emulator strategies. Two broad strategies exist for building emulators. One is to construct a general-purpose emulator of the climate system and then apply it to specific problems. However, as shown by Van Loon et al. (2025) [37] in the context of the ACE2 emulator and the pattern effect, this strategy may not always succeed. A second, more targeted approach for large-scale climate dynamics is to design an emulator tailored to a given problem, e.g. [5]. While this sacrifices generality, it offers key advantages: clarifying the choice of variables and scales to model, grounding the design in physical intuition and prior literature, and isolating only the processes most relevant to the problem. This focus also enhances interpretability and helps bridging the gap between simulation and understanding [101].

B. A reduced order model of surface temperature and radiative fluxes

We aim to build a skillful emulator of large-scale sea surface temperature (SST) and radiative fluxes capable of capturing both stationary and perturbed statistics. Building on the previous sections, we adopt the following functional form for the neural model:

$$d\mathbf{x} = (\mathbf{L}\mathbf{x} + \mathbf{n}(\mathbf{x}))dt + \boldsymbol{\Sigma}(\mathbf{x})d\mathbf{W}, \quad (11)$$

Where \mathbf{W} is the standard Wiener process. As before, to improve readability we refer to Appendix C for technical details.

As outlined throughout the paper, a central challenge lies in selecting preprocessing steps to define the coarse-grained dynamics \mathbf{x} to be modeled. These choices are critical for identifying the proper variables, since the climate system involves not only SST and radiative fluxes but also many other interacting variables. This is thus a practical instance of a partially observed state vector. Below, we describe the dataset and preprocessing procedure, which largely follows [102], with further details provided in that work.

1. Data, preprocessing and the choice of proper variables

a. Data. We consider outputs from the state-of-the-art coupled climate model GFDL-CM4 [103], which provides a 600-year pre-industrial control run with constant CO_2 . The ocean component is MOM6 [104] with 0.25° horizontal resolution and 75 vertical layers, and the atmosphere is AM4 [105, 106] with 100 km resolution and 33 vertical layers. The model in Eq. (11) is trained on this control run. We consider two climate fields: sea surface temperature (SST) and the global mean net radiative flux at the top of the atmosphere (TOA). The SST field is restricted to latitudes $[-45^\circ, 45^\circ]$, following earlier studies that highlight the importance of radiative feedbacks in the tropics and subtropics [39, 97].

b. Choosing the proper variables. Climate dynamics involves many interacting fields beyond SST and radiative fluxes. Our goal is a reduced-order model that captures the coarse-grained dynamics while representing unresolved processes as noise. We coarse-grain the GFDL-CM4 control run in space and time, averaging daily data to monthly means and removing the seasonal cycle to focus on anomalies rather than periodic signals driven by solar forcing. Considering 1 month averages in TOA fluxes is not arbitrary: the immediate response of TOA fluxes to perturbations in SST is fast (e.g., ~ 20 days in tropical large-scale convective overturning motion in the GFDL-CM4 model) [102]. This averaging filters out higher-frequency processes that mediate surface–TOA coupling, yielding a system that is more

Markovian. Given so, *direct* causal links between TOA fluxes at SST patterns can be detected as one time step responses; see Appendix A. We then high-pass filter with a cut-off of 10^{-1} years, removing (i) low-frequency (multidecadal) oscillations, which are poorly sampled even in 600-year runs, and (ii) slow drifts from incomplete ocean equilibration. This choice sacrifices the ability to capture multidecadal processes but ensures robust sampling of subdecadal statistics, yielding a larger effective sample size. Implicitly, the choice assumes that the response of the net radiative flux to SST perturbations occurs within a 10-year window. Next, we decompose the SST field $\mathbf{X}(t) \in \mathbb{R}^N$ into empirical orthogonal functions (EOFs):

$$\mathbf{X}(t) = \sum_{i=1}^n x_i(t)\mathbf{e}_i + \sum_{j=n+1}^N y_j(t)\mathbf{e}_j, \quad (12)$$

and retain the first $n = 20$ modes $x_i(t)$. The combined steps of monthly averaging, high-pass filtering and projection over EOF bases define a coarse-grained system for the slow SST variability. This choice follows earlier work showing the skill of linear Markov models built on similar preprocessing [4, 5]. For radiative fluxes, we focus on the global mean TOA net flux, as the TOA flux exhibits little spatial structure and we are mainly interested in its average value. The state vector is then defined as $\mathbf{x}(t) \in \mathbb{R}^{n+1}$, consisting of the n SST principal components concatenated with the global mean TOA flux.

c. Forced simulations We test the model’s ability to reconstruct changes in global-mean TOA radiative flux given prescribed SST trajectories from two 150-years long forced runs: 1pctCO₂ and 4×CO₂. The 1pctCO₂ experiment imposes a 1% CO₂ increase per year starting from pre-industrial conditions, while the 4×CO₂ experiment abruptly quadruples CO₂ at $t = 0$. A complication is that TOA fluxes respond directly to rising CO₂, whereas our reduced-order model only uses SST and fluxes and does not explicitly include CO₂. To address this, we remove the portion of change of the net TOA radiative flux that is attributable solely to rising CO₂. This allows us to isolate and study the component of radiative feedback that is driven by changes in SST. This correction exploits the logarithmic dependence of global-mean forcing on CO₂ concentration [107, 108]. As is standard, we subtract 8Wm^{-2} in the 4×CO₂ run [109], and apply a time-dependent correction $\alpha \log(C_t/C_0)$ in the 1pctCO₂ run, where C_t and C_0 denote CO₂ concentrations in the forced and control simulations.

2. Stationary statistics and forced responses

a. Stationary statistics. Given the $n + 1$ dimensional state vector $\mathbf{x}(t) \in \mathbb{R}^{n+1}$ defined above, we train the emulator in Eq. (11) on the long control run of GFDL-CM4. The trained model is then used to simulate

a trajectory of equal length (i.e. 600 years at monthly time step). The stationary probability distributions of the leading SST mode and the net radiative TOA flux are well reproduced (Fig. 6a,b). The main discrepancies arise in the autocorrelation functions, shown for the first SST mode (closely linked to ENSO [110]) and the TOA flux.

b. Forced responses. The pattern-effect problem (Section IV A) concerns identifying causal links between SST warming patterns and TOA flux changes. Before using our emulator for Green’s function-like studies to investigate the pattern-effect, we first assess its skill as a reconstruction tool. Specifically, we reconstruct global-mean TOA flux from prescribed SST trajectories in the two forced experiments, i.e. 1pctCO₂ and 4×CO₂. Forced SSTs are projected onto the first $n = 20$ EOFs from the control run, yielding coarse-grained trajectories $\mathbf{x}_{\text{SST}}^f(t)$, f denotes “forced.” Given $\mathbf{x}_{\text{SST}}^f(t)$, the emulator returns the TOA variable $x_{\text{TOA}}(t + 1)$ at the next time step, initialized with $x_{\text{TOA}}(0) = 0$. Results (Fig. 6e,f) show that the emulator largely reproduces TOA flux changes in both scenarios. This reconstruction is possible because we focus on one-month averages, which reduce the time-dependent TOA response, driven by an atmospheric reorganization at sub-monthly scales, into a one-step prediction. For the 1pctCO₂ experiment, the linear trend in net TOA flux is $-0.043\text{Wm}^{-2}\text{yr}^{-1}$ in GFDL-CM4 and $-0.034\text{Wm}^{-2}\text{yr}^{-1}$ in the emulator. We then compute correlations between reconstructed and simulated radiative flux at the TOA, after removing a linear trend in 1pctCO₂ and an initial 50-year transient in 4×CO₂. At monthly resolution, correlations are $r = 0.37$ (1pctCO₂) and $r = 0.43$ (4×CO₂). If yearly averages are considered (as in the current literature, see e.g. [38]) these increase to $r = 0.70$ (1pctCO₂) and $r = 0.74$ (4×CO₂). All correlations are significant at the 5 sigma level under a null hypothesis of zero correlation, tested via bootstrap resampling with replacement.

3. Interpretability and understanding: ensemble mean and variance responses

In the previous section, we showed that the reduced-order neural emulator can reconstruct the net radiative flux at the top of the atmosphere (TOA) from prescribed changes in the sea surface temperature (SST) field. This amounts to the mapping $\mathbf{x}_{\text{SST}}^f(t) \rightarrow x_{\text{TOA}}(t + 1)$, where $\mathbf{x}_{\text{SST}}(t) \in \mathbb{R}^n$, $x_{\text{TOA}}(t) \in \mathbb{R}$, and $x_{\text{TOA}}(0) = 0$. We now ask the following question: *What are the SST patterns that contribute the most to this skillful prediction?* Addressing this question requires moving beyond prediction to identify the causal influence of individual SST components on radiative flux. We frame the problem in terms of linear response theory, focusing on the direct link $x_{j,\text{SST}}(t) \rightarrow x_{\text{TOA}}(t + 1)$, where $x_{j,\text{SST}}(t)$ denotes the j -th SST component.

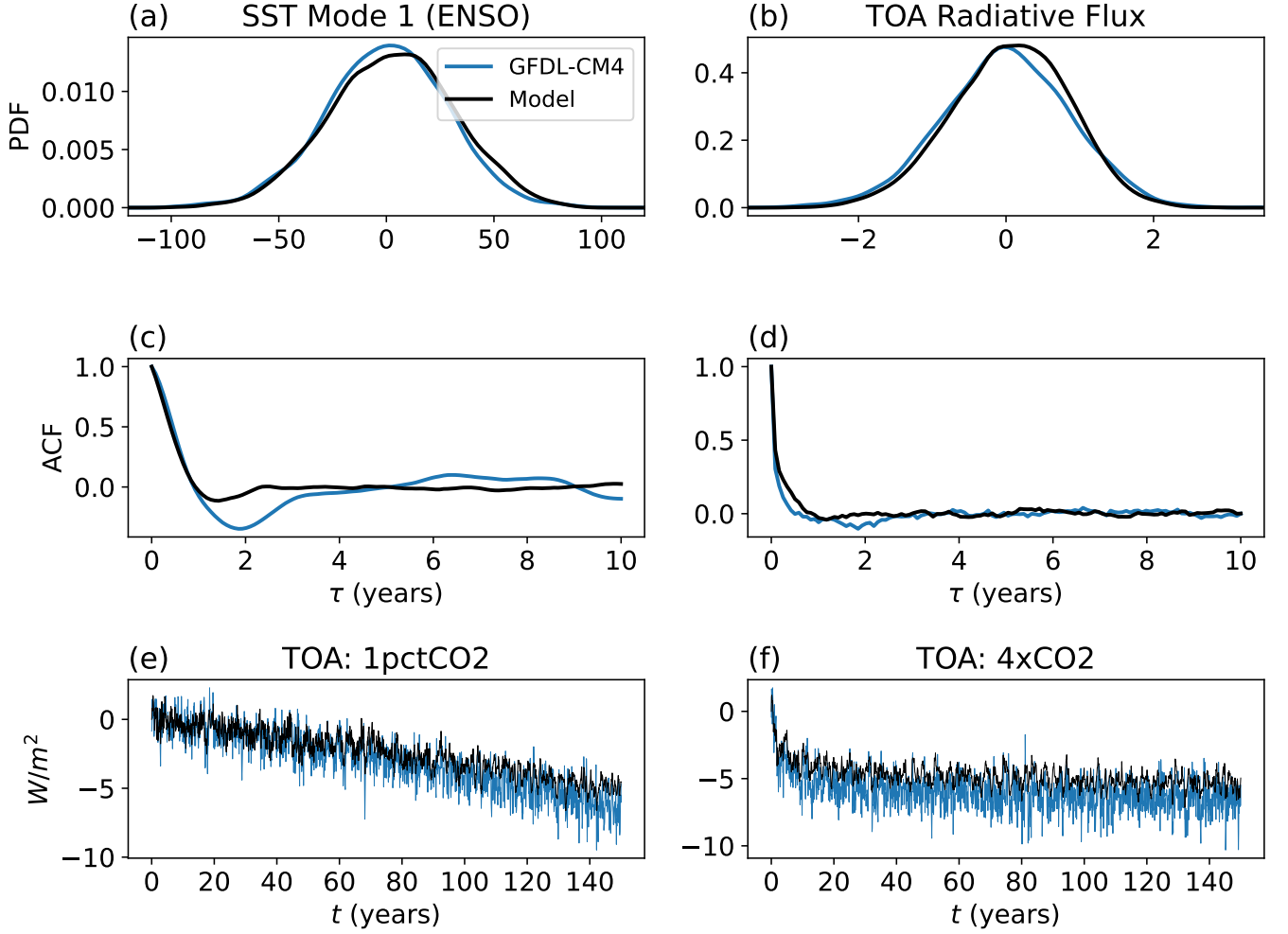


FIG. 6: Panel (a): stationary distributions obtained for the 1st principal component of the sea surface temperature (SST) field as in the original GFDL-CM4 climate model and as emulated by the neural emulator with multiplicative noise in Eq. (11). Units: nondimensional. Panel (b): same as panel (a) but for the global mean radiative flux at the top of the atmosphere (TOA). Units: W/m^2 . The stationary distributions have been obtained after simulating the neural emulator for 600 years. Second row: same as the first row but for the autocorrelation functions. Third row: reconstruction of the net radiative flux at the TOA by the neural emulator in Eq. (11) after constraining the SST degrees of freedom to follow a precomputed trajectory in two forced experiments in the GFDL-CM4 model. The forced experiments considered are the 1pctCO₂ and 4×CO₂, see Section IV B 1 for details. Note: the net flux at the TOA variable is negative upward (i.e., leaving the planet).

a. Response in ensemble mean. To quantify this link, we perturb the emulator in Eq. (11) following the procedure in Appendix A. Briefly, at $t = 0$, we apply a small impulse $\Delta_j = 10^{-2}\sigma_j$ to the j -th SST component, with σ_j its stationary standard deviation. We then compute the ensemble-mean response of the net TOA flux at $t = 1$, denoted $\delta\langle x_{\text{TOA}}(1) \rangle$. This quantity, referred to as $R_{\text{TOA},j}^{\mu}(1)$, represents the ensemble-mean response (μ indicates the mean) and is estimated over 10^6 initial conditions to ensure robust statistics

b. Response in ensemble variance. While the ensemble-mean response is informative, it captures only part of the adjustment. Large-scale climate responses can involve shifts of probability distributions. To partially account for this, we quantify the response in the variance of the net TOA radiative flux to surface warming perturbations. As above, the estimate is based on an ensemble of 10^6 trajectories. For consistency in physical units, we express the response in terms of standard deviation rather than variance, denoting it by $R_{\text{TOA},j}^{\sigma}(1)$ (σ indicates the standard deviation). This quantity measures the change in ensemble spread following a perturbation of the j -th SST component.

Conceptually, this procedure provides a computationally efficient analogue of atmospheric-only Green's function experiments, while shifting the focus from individual trajectories to full probability distributions.

c. Sensitivity maps. The vectors of one-time-step responses in mean and standard deviation, \mathbf{R}^μ and \mathbf{R}^σ , are projected back to the full N -dimensional SST field using the EOFs, $\mathbf{e} \in \mathbb{R}^{n,N}$:

$$\mathbf{S}^{\mu,\sigma} = \mathbf{R}_{\text{TOA}}^{\mu,\sigma}(1) \cdot \mathbf{e} = \sum_j^n R_{\text{TOA},j}^{\mu,\sigma}(1) \mathbf{e}_j, \quad (13)$$

where $\mathbf{S}^\mu, \mathbf{S}^\sigma \in \mathbb{R}^N$ represent sensitivity maps in mean and standard deviation, respectively. At each ocean grid point i , these maps approximate the sensitivities $\frac{\partial x_{\text{TOA}}^{\mu,\sigma}}{\partial x_{\text{SST},i}}$, where x_{TOA}^μ and x_{TOA}^σ respectively represent the ensemble mean and standard deviation of the mean, net radiative flux and $x_{\text{SST},i}$ is the SST at location i .

The sensitivity maps in mean (\mathbf{S}^μ) and standard deviation (\mathbf{S}^σ) are shown in Figure 7. The obtained sensitivity map \mathbf{S}^μ is in qualitative agreement with previous results in response theory (Figure 2(a) in [102]), with other data-driven approaches (see Figure 7(b) in [111] and Figure 2 in [112]), but, most importantly, with the sensitivity map obtained by directly perturbing the SST boundary condition of atmosphere-only climate models (see third row of Figure 2 in [38], see Figure 5(a) in [39]). In the latter case, the maps exhibit fewer spatial features due to the coarse resolution of the perturbation patches (spanning tens of degrees) in numerical models experiments.

The dominant feature of \mathbf{S}^μ is a dipole in the tropical Pacific: negative sensitivity in the west and positive sensitivity in the east [39]. This implies that eastern Pacific warming produces a positive radiative feedback, while western Pacific warming produces the opposite. The mechanisms are well established [100, 113]: in the east, high climatological low-level cloud cover decreases under warming, reducing reflected shortwave radiation and yielding positive sensitivity. In the west, deep convection transports surface warming vertically and then horizontally via gravity waves, strengthening the inversion over the eastern Pacific and other stratocumulus regions, increasing low-level cloud fraction and reflected shortwave radiation, thus producing a negative feedback. This analysis confirms that the accurate reconstructions in the forced regime (Fig. 6e,f) arise from physically consistent mechanisms, and that coarse-grained neural models can recover such causal linkages.

Finally, the variance response \mathbf{S}^σ (Fig. 7b) highlights regions where perturbations alter the spread of radiative responses across ensemble members. Perturbations in stratocumulus-dominated regions (northeast Pacific, off

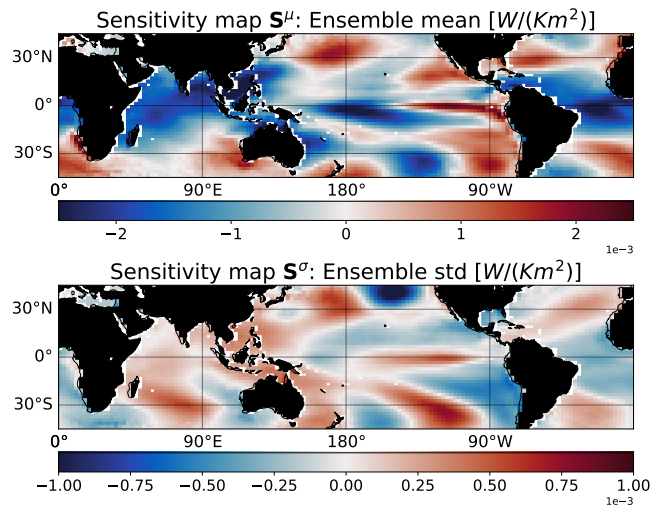


FIG. 7: Sensitivity maps obtained using the neural emulator in Eq. (11). At each SST grid point i , we show the one-time-step response in the ensemble mean (\mathbf{S}^μ) and ensemble standard deviation (\mathbf{S}^σ) of the global-mean net radiative flux at the TOA following an impulse perturbation in SST at that location. The computation is carried out in a 21-dimensional reduced space spanned by empirical orthogonal functions, and the maps represent the projection of these low-dimensional results back to the full grid. Responses are estimated from an ensemble of 10^6 initial conditions.

the coast of South America) yield negative variance responses: the ensemble distribution of net radiative flux narrows relative to the control, highlighting small uncertainties in the mean response studied above. By contrast, surface warming perturbations in the central and western Pacific lead to positive variance responses, reflecting a broader spread of the net radiative flux distribution after SST perturbations. To our knowledge, such variance responses have not been quantified before. Unlike the response in the mean, which has been examined extensively and shows broad agreement across atmospheric models [38], the response in ensemble variance has no established benchmark. Because it reflects changes in variability, it may differ significantly across atmospheric models. Moreover, estimating such responses requires very large ensembles, which are prohibitively expensive in conventional climate models. For this reason, the results presented here should be viewed as an exploratory step: they highlight potentially important regional structures, but a full climate interpretation will require systematic inter-comparison and validation against other modeling frameworks, such as novel data-driven tools to estimate response through the fluctuation-dissipation theorem [114].

4. Main takeaways

In this Section, we developed a stochastic neural emulator that captures the joint evolution of the sea surface temperature (SST) field and the global mean net radiative flux at the top of the atmosphere (TOA) in the GFDL-CM4 climate model. Addressing a specific, well-posed problem, proved crucial in guiding the construction of the model: it enabled us to build on previous literature, restrict attention to just two variables and a limited range of spatial and temporal scales. These simplifications led to a stable and computationally efficient emulator that responds to external forcing and can be used to investigate causal relationships via perturbation experiments. Such experiments focused on very large ensembles (10^6 trajectories), currently impossible to perform with climate models. These results demonstrate that reduced-order neural emulators can extend beyond reproducing stationary climate dynamics to enable efficient, ensemble-based perturbation experiments.

V. DISCUSSION AND CONCLUSION

In summary, the first part of this work discussed the limitations of purely data-driven models of complex climate systems. We highlighted the potential of combining traditional reduced-order modeling approaches, including state-dependent (multiplicative) stochastic parameterizations, with recent advances in neural networks to study large-scale, low-frequency climate dynamics. We emphasized the need to evaluate such models against both stationary and perturbed statistics. In this context we discussed how response theory provides rigorous guidance to move beyond stationary evaluation and probe causal mechanisms. These ideas were then illustrated through a climate-dynamics problem focusing on inferring causal relations between surface warming and changes in net radiative fluxes. Given careful variable selection, reduced-order neural stochastic models can capture both stationary and perturbed statistics in a computationally efficient way. Below, we expand on these points and outline directions for future work.

A. Limits of data-driven-only climate emulators and the role of stochastic approaches

In the first part of this paper, we distinguished two possible scenarios in data-driven modeling:

- i. *Unknown equations, fully observed state vector.* In this idealized setting, it is possible to infer a model from data alone that reproduces the system’s stationary statistics and responds accurately to small external perturbations.
- ii. *Unknown equations, partially observed state vector.* This more realistic case presents fundamental dif-

iculties, even with access to high-quality data and powerful neural models architectures. The model skill now depends critically on two factors: (a) the choice of variables to model and (b) how unobserved degrees of freedom are parameterized.

These results highlight intrinsic limitations of purely data-driven-only modeling in high-dimensional climate systems, where the full set of relevant variables is typically unknown and no rigorous framework exists for selecting the proper variables to model. By *variable selection* we mean the choice of climate fields as well as their spatial and temporal scales (also including dimensionality reduction methodologies). Such choices are guided by the physical process of interest, and in the case of low-frequency climate dynamics, they motivate the development of reduced-order neural emulators tailored to specific phenomena as efficient alternative to general purpose emulators. A central challenge is to parameterize the cumulative effect of unresolved degrees of freedom. Model performance (especially in capturing responses to external forcings) depends critically on this choice and we showed that multiplicative (state-dependent) noise is preferable to additive noise.

We emphasize that the analysis presented here applies to data-driven models of turbulent geophysical systems that must capture both stationary statistics and responses to external perturbations, as in (causal) Green’s function experiments [38]. For Earth system models, these issues mainly concern autoregressive *climate emulators*, particularly coupled atmosphere–ocean systems, and should not be confused with short-term weather forecasting using neural networks (e.g., [23, 115]), where long-term stability and forced responses are less relevant. Our study also does not address statistics-based emulators for climate change projections, which have proven effective for investigating responses of key climate variables to CO₂ forcing [116, 117]; see [116] for an example where simple approaches, such as linear pattern scaling, can outperform more complex models.

Future work. The discussion above suggests two possible directions for future research in autoregressive emulators of climate. First, a stochastic formulation of neural autoregressive climate emulators is preferable to a purely deterministic one. Probabilistic formulations align more closely with the inherently stochastic and uncertain nature of climate dynamics [118]. Recent advances in weather emulation already point in this direction such as FourecastNet3 [23], GenCast [23] and the novel work of Alet et al. (2025) [119]. Second, the ability of climate emulators in capturing forced responses in the full probability distribution, akin to Green’s function experiments, remains largely unexplored. A promising way forward is to evaluate novel architectures on their ability to respond to external perturbations on a hierarchy of simplified models relevant to geophysical fluid dynamics, such as the Lorenz–96 system [120]. These controlled testbeds en-

able rigorous quantification of forced responses and could inform the design of future architectures for data-driven climate modeling.

B. Response theory as a theoretical framework for model evaluation

We argued that the impulse response operator is a building block that a model should capture in order to reproduce causal interactions across degrees of freedom and to accurately respond to external perturbations (Section II B and Appendix A). This perspective enables us to move beyond evaluation metrics based solely on stationary statistics and instead consider the effect of external interventions. Assessing impulse responses is straightforward in the case of data-driven emulators built from simple numerical models, i.e. models that allow us to simulate thousands of ensemble members, as in the first part of this study. In such cases, one can actively perturb the reference model to generate a ground truth for the response operator. However, for models constructed from observational data, such direct perturbations are not possible. In this context, one could, in principle, leverage the Fluctuation-Dissipation Theorem (FDT) to predict the response operator from data alone [17, 81]. Traditionally, the quasi-Gaussian approximation have yield reliable estimates of impulse responses in the ensemble mean [47, 121]. Recent advances in score-based generative models have shown the potential to extend these predictions to responses in higher-order moments [114].

Future work. In the absence of direct perturbation experiments, FDT provides a rigorous bridge between stationary and forced dynamics [48, 49]. With sufficiently long integrations of current climate emulators, one can readily focus on representative large-scale modes and estimate their impulse responses from the stationary record, thereby extending evaluation beyond stationary statistics with minimal computational cost. A recent example illustrating this approach in the climate context can be found in [18]. Moreover, the response operator at the shortest time step encodes *direct* causal links, i.e. the input-output relationships across variables in a reduced-order emulator (see Appendix A). Future work will leverage this information to suppress spurious, non-causal input-output dependencies during training, similarly to the recent work of Chen and Liu (2024) [59] on causally constrained, sparse reduced-order models.

C. A realistic application: radiative responses to temperature perturbations

Building on the theoretical insights introduced in the first part, the second part of the paper presented a stochastic neural emulator for the coarse-grained

dynamics of sea surface temperature (SST) and net radiative flux at the top-of-atmosphere (TOA). The model was trained on a long unforced simulations of a coupled climate model and designed with a specific physical task in mind: capturing radiative feedbacks to SST anomalies. The emulator focuses on the evolution of 20 principal components of the SST field and on the scalar global mean, net radiative flux; unobserved degrees of freedom are parametrized through multiplicative noise through an additional neural network. The emulator largely reproduces the stationary statistics of the system and, more importantly, allows us to reconstruct TOA radiative fluxes in two forced simulations. We inferred the direct causal links between temperature modes and TOA fluxes through a perturbation approach, akin to Green’s function-like experiments with climate models [38], targeting the so-called “pattern effect” [39]. Crucially, the analyses targeted both responses in the ensemble mean and variance. Such responses are then projected back onto the EOFs to obtain maps of sensitivity in mean and variance change of the radiative flux at the TOA to SST warming perturbations. We argued that the sensitivity map for the ensemble mean is consistent with recent studies, indicating that the emulator’s skill in reconstructing TOA fluxes under forcing arises from physically meaningful mechanisms. In contrast, the sensitivity map of the ensemble variance is a novel result, not previously examined in the literature. It highlights the potential for uncertainty quantification in perturbation experiments but it requires further investigation to better understand the underlying physical mechanisms. These findings highlight the potential of reduced-order neural emulators to perform thousands of perturbation experiments, shifting the focus of climate feedback analysis from mean responses to the responses of probability distributions.

Modeling the climate system from data alone is constrained by observing only a subset of variables of a multiscale, high-dimensional dynamical system. This raises the fundamental challenge of identifying the appropriate variables (both fields and spatiotemporal scales) a fundamental problem in physics, emphasized in classical work [122] and revisited in recent studies [123]. However, large-scale climate dynamics is often well characterized by a few recurrent spatiotemporal patterns, or modes of variability. In this case, the multiscale structure of the climate system can be an advantage allowing us to derive data-driven models of the coarse-grained dynamics while treating unresolved, fast processes stochastically. Traditional reduced-order models stand out from general-purpose emulators by targeting specific climate problems from the outset, guided by prior literature, physical insight, and a clear understanding of the relevant variables and scales at play. Such data-driven modeling approach has a long history in climate science [2], though most efforts have emphasized reproducing stationary statistics or short-term forecasting [3, 4, 75] rather than forced

responses. A promising perspective is to build on such established reduced-order approaches, focusing on powerful neural networks to fit deterministic and stochastic components and on tools from response theory, such as the FDT, to guide model development. Together, these strategies can enable efficient algorithms to study how full probability distributions respond to external perturbations, opening new avenues for causal inference and attribution in climate science.

Appendix A: Response operator: practical estimation and causal interpretation

1. Inferring the response operator in practice

Given a model $d\mathbf{x} = \mathbf{f}(\mathbf{x})dt + \Sigma(\mathbf{x})d\mathbf{W}$ we build the impulse response operator as follows:

1. We simulate a very long trajectory of the model, starting from a random initial condition and remove an initial transient. We then sample N_e random points from the simulation to define an ensemble of N_e initial conditions on the model's attractor. N_e should be very large (i.e. $N_e \gg 1$) in order to sample the whole attractor and approximate averages over the invariant distribution.
2. For each one of the N_e initial conditions, we impose an impulse perturbation $x_j(0) \rightarrow x_j(0) + \Delta_j \delta(t)$ of size Δ_j on the j -th degree of freedom at time $t = 0$. $\delta(t)$ is the Dirac delta function. The amplitude Δ_j should be theoretically infinitesimally small, ensuring linearity of the response even in nonlinear systems. In practice we do as follows: we consider the long time series of $x_j(t)$ from the long control integration above and define $\Delta_j = 10^{-2}\sigma_j$, where σ_j is the standard deviation of time series $x_j(t)$.
3. Therefore, for a given initial condition $\mathbf{x}(0)$, we simulate two trajectories: a control trajectory without perturbation and a perturbed one, where an impulse perturbation Δ_j has been imposed on the j -th degree of freedom at time $t = 0$. This procedure is repeated in parallel for all initial conditions, resulting in an ensemble of N_e paired of control and perturbed trajectories.
4. At each time t we then estimate the time dependent ensemble average $\langle A(x_k(t)) \rangle$ of an observable $A(x_k(t))$ for both the perturbed and unperturbed run. We refer to the perturbed and control ensemble average respectively as $\langle A(x_k(t)) \rangle_p$ and $\langle A(x_k(t)) \rangle$. The observables considered in this study are going to be: (i) $A(x_k(t)) = x_k(t)$ and (ii) $A(x_k(t)) = (x_k(t) - \mu_k(t))^2$, with $\mu(t)$ representing the time-dependent mean of the distribution, therefore quantifying the response in ensemble mean and variance.
5. We define the impulse response operator for observable $A(x_k(t))$ as

$$R_{k,j}(t) = \frac{\langle A(x_k(t)) \rangle_p - \langle A(x_k(t)) \rangle}{\Delta_j}.$$

2. Causal interpretation of the response operator

Causality in natural systems is inferred through external interventions: an agent perturbs the system

and the response is measured [77, 78]. Climate modeling follows the same principle through Green's function experiments, where one variable is perturbed and the response of another is evaluated [38, 124]. Linear response theory formalizes this principle, providing a rigorous framework for causal analysis both in models and directly from data [17, 18, 114].

Because responses are inherently time-dependent, causal links through responses can be distinguished in three forms, all encoded in the time-dependent response operator: (i) direct links, (ii) indirect links, and (iii) cumulative links (or causal sensitivity). In what follows, we use the triad system in Eq. (6) as a simple example to illustrate these ideas in a clear and unambiguous way. Finally, we summarize recent approaches for estimating responses directly from data and refer to Baldovin et al. (2020) [17] for details on the theoretical foundations of this approach.

Consider a N dimensional dynamical system of the kind:

$$\frac{dx_i}{dt} = f_i(x_1, x_2, \dots, x_N); \text{ with } i = 1, 2, \dots, N. \quad (\text{A1})$$

For stochastic systems, causal links are contained in the deterministic drift f_i , so the discussion below applies to both deterministic and stochastic dynamics. In this setting, the existence of a direct *causal* link $x_j \rightarrow x_k$ is determined by whether x_j appears in the arguments of f_k . More formally, the *absence* of a direct causal link $x_j \rightarrow x_k$ is expressed by:

$$\frac{\partial f_k}{\partial x_j} = 0.$$

As a concrete example, we return to the triad system in Eq. (6), for which the underlying direct causal links are known exactly. This example provides a straightforward, intuitive illustration of how perturbation experiments reveal causal interactions. Figure 8 reports both (a) its functional form and (b) its causal graph, which encode the same information. Causal relations can then be probed by adding independent impulse perturbations to each degree of freedom and record the system's response. Responses are computed up to a long time horizon τ_{\max} , with discrete times $t = 0, dt, 2dt, \dots, \tau_{\max}$. Since we are interested in causal relations, it suffices to consider the identity observable $A(x_k(t)) = x_k(t)$, i.e. the response of the ensemble mean [17]. We now clarify the three different types of causal links mentioned at the start of this Section.

Direct causal links. The direct causal links are encoded in the response operator $\mathbf{R}(dt)$ evaluated at the shortest time step $t = dt$. The intuition follows directly from the graph representation in Fig. 8(b) and is rather straightforward.

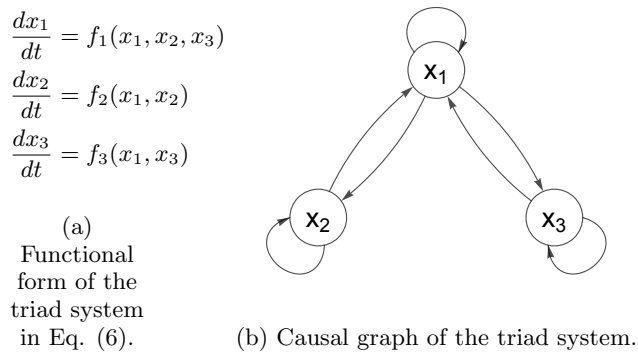


FIG. 8: Panel (a) Functional form of the triad system in Eq. (6). Panel (b) Graph structure of the triad system. Note from panel (b) that causality in dynamical systems can involve cycles, in contrast with the acyclic structures often assumed in applications outside physics, see e.g. [125].

- Any perturbation applied to x_2 will affect x_2 itself and x_1 after one time step, but not x_3 . Hence, we infer $\partial f_3/\partial x_2 = 0$.
- A perturbation applied to x_3 will affect x_3 and x_1 , but not x_2 , so $\partial f_2/\partial x_3 = 0$.
- By contrast, a perturbation to x_1 propagates to all three variables within a single step, indicating direct causal links from x_1 to both x_2 and x_3 .

Indirect causal links. Causal relations in physical systems extend beyond direct interactions. A variable x_j may affect another variable x_k indirectly through an intermediate variable x_i , forming a pathway $x_j \rightarrow x_i \rightarrow x_k$. Such indirect links are central in climate dynamics [126] and in complex systems more broadly [127]. Within the response framework, these pathways are revealed by the time-dependent operator $R_{k,j}(t)$: the first non-zero response identifies the shortest causal path in the graph connecting x_j to x_k . Crucially, if $R_{k,j}(t) = 0$ for all time t , then no external intervention on x_j can ever influence the behavior of x_k .

Cumulative causal links or causal sensitivity. Finally, Baldovin et al. [17] introduced a cumulative (in time) measure of causation between two variables, defined as $D_{k,j} = \int_0^{\tau_{max}} R_{k,j}(t) dt$. Such cumulative link, can be also referred to as “causal sensitivity”. Such a measure is especially relevant in practical experiments with high-dimensional models where interactions unfold across multiple spatial and temporal scales. A concrete example using climate models, is provided by the approach of Bloch-Johnson et al. (2024) [38], where causal links are inferred between patterns of surface warming and the net radiative flux at the top of the atmosphere. Their method reconstructs responses to perturbations by: (i) applying surface warming perturbations, (ii)

integrating an atmospheric-only model with and without the perturbation, and (iii) computing the average (in time) difference between the two runs after removing an initial transient. In this case, the causal link emerges precisely as a cumulative (in time) atmospheric response to the surface perturbations.

We emphasize the crucial role of ensemble averages in establishing the general validity of response theory. Evaluating responses along single trajectories of nonlinear systems is strongly affected by chaos, restricting the applicability of these ideas to short times and very small perturbations. In contrast, focusing on observables, i.e. quantities averaged over the invariant density, ensures the robustness of the theory and largely removes the dependence on chaos. For a detailed discussion of this point, we refer the reader to [128]. Future efforts to estimate responses in climate science, which often rely on perturbing single trajectories, would therefore benefit from focusing on ensemble-averaged observables.

Response operator from data alone. Given the assumption of Markovianity it is possible to infer the system’s response operator from a long stationary trajectory using the Fluctuation-Dissipation Theorem (FDT) [17]. The FDT formula provides a link between stationary and perturbed dynamics by predicting forced responses from stationary statistics alone [129]. Specifically:

$$R_{k,j}(t) = -\left\langle A(x_k(t)) \frac{\partial \ln \rho(\mathbf{x})}{\partial x_j} \Big|_{\mathbf{x}(0)} \right\rangle, \quad (\text{A2})$$

where $A(x_k(t))$ is a general observable, $\rho(\mathbf{x})$ is the stationary distribution. $\langle \cdot \rangle$ refers to ensemble average, approximated through temporal averages. $\frac{\partial \ln \rho(\mathbf{x})}{\partial x_j} \Big|_{\mathbf{x}(0)}$ represents the so-called “score function” evaluated at the initial state, i.e. on the attractor [15]. Therefore, in principle the response operator can be computed from data if the score $\nabla \ln \rho(\mathbf{x})$ is available. In practice, the score is often inaccessible, and most applications rely on the quasi-Gaussian (qG) approximation, by replacing $\rho(\mathbf{x})$ with a Gaussian distribution $\rho^G(\mathbf{x})$ with same mean and covariances [48, 130]. For responses in the ensemble mean—which are sufficient to infer causal links—the qG approximation achieves high skill even for nonlinear systems [17, 114, 121]. Recent work [114] has demonstrated that generative modeling techniques can be used to efficiently estimate the score directly from data, leading to high skill in computation of higher-order responses (up to the 5th moment) in strongly nonlinear regimes. Other fruitful avenues lie in frameworks at the intersection of Markov State Modeling and Koopman operator theory such as [131].

It is worth emphasizing that the central limitation discussed in the main text, i.e. the need to choose the proper variables, remains relevant for the inference of response operators via FDT as well (and for any causal inference

methodology); see the discussion in [17].

Appendix B: Relevance of the the triad system for geophysical turbulence

Here, we motivate the choice of the triad model analyzed in Section III as a building block for geophysical turbulent flows. We further present and test the associated analytical stochastic model for the slow variable x_1 (as discussed in Section III C 1), illustrating that Markovian reduced-order models can sometimes be derived from partial observations. For detailed mathematical derivations and additional examples, we refer to the original work by Majda and collaborators [16, 46, 48, 60, 61].

1. Link to geophysical turbulence

Projecting many geophysical turbulent flows, such as quasigeostrophic models, onto a complete set of orthogonal basis functions (spectral or empirical modes such as EOFs), give rise to the following generic form for the mode amplitudes:

$$d\mathbf{u}/dt = \mathbf{F} + \mathbf{L}\mathbf{u} + \mathbf{B}(\mathbf{u}, \mathbf{u}), \quad (\text{B1})$$

where \mathbf{F} is an external forcing, \mathbf{L} is a linear operator and $\mathbf{B}(\mathbf{u}, \mathbf{u})$ is a nonlinear, quadratic operator. The linear operator $\mathbf{L} = \mathbf{L}' + \mathbf{D}$, is formed by a skew-symmetric operator \mathbf{L}' and by a diagonal dissipation matrix \mathbf{D} with negative real entries. The quadratic nonlinearity should be energy-conserving, satisfying $\mathbf{u} \cdot \mathbf{B}(\mathbf{u}, \mathbf{u}) = 0$ [48, 60, 132]. Eq. (B1) is the typical abstract form of dry cores of atmospheric models [67]. Galerkin truncations of turbulent systems often reduce to this structure, as in the Lorenz '63 and Charney–DeVore models [68, 132, 133]. $\mathbf{u} \in \mathbb{R}^N$ represents the full turbulent geophysical system, with N infinite in principle and finite but very large in applications ($N \gg 1$). The state \mathbf{u} is then decomposed into slow and fast components, $\mathbf{u} = (\mathbf{x}, \mathbf{y})$, i.e. \mathbf{x} will represent the first n components of \mathbf{u} and \mathbf{y} the next $N - n$.

We consider the simple case of $N = 3$: one large-scale resolved mode x_1 and two fast modes $\mathbf{y} = (x_2, x_3)$. Majda and collaborators [46] considered an exact projection of the slow mode x_1 and the two fast modes (x_2, x_3) onto the dynamics in Eq. (B1). This gives rise to three equations, defined by a forcing term, linear and quadratic self- and cross-interaction across slow and fast time scales. The triad model in Eq. (6) is then obtained by approximating the quadratic self-interactions of the fast modes as a damping and stochastic forcing, as: $-\gamma_i \epsilon^{-1} x_i + \sigma_i \epsilon^{-1/2} \xi_i$, with $i = 2, 3$. ξ_i is a standard Gaussian white noise process. ϵ sets the time-scale separation between the slow and fast modes. The key assumption is that the detailed nonlinear self-interactions among fast modes are not

important if the goal is to capture the coarse-grained slow dynamics. This approximation transforms the original deterministic equations into a stochastic system. The specific version used in Eq. (6) is further simplified by setting to zero a few interactions, such as the linear cross- and self-interactions of the fast modes as well as the external forcing terms.

Therefore, the relevance of the triad system (Eq. (6)) to this study is that it provides a minimal multiscale setting with linear and quadratic nonlinear interaction of the kind that naturally arise when geophysical turbulent flows are expressed in terms of orthogonal bases such as EOFs. For additional details see also Section 4 of [16].

2. Analytical stochastic model for the slow variable x_1

Starting from the triad model in Eq. (6), Majda and collaborators [60] showed that an analytical reduced-order equation for the slow variable x_1 can be rigorously derived in the limit $\epsilon \rightarrow 0$ using standard projection techniques [46–48]. The mode reduction predicts the functional form of the dynamics governing the resolved, slow variable [60–63]. The resulting stochastic equation is

$$dx = (\tilde{F} + ax + bx^2 - cx^3) dt + (A - Bx) dW_2 + \sigma dW_3, \quad (\text{B2})$$

where the coefficients are expressed in terms of parameters of the triad system in Eq. (6) as: $a = L_{11} + \epsilon(\frac{L^2 \sigma_2^2}{2\gamma_2^2} - \frac{L_{12}^2}{\gamma_2} - \frac{L_{13}^2}{\gamma_3})$; $b = -2\epsilon \frac{L_{12}L}{\gamma_2}$; $c = \epsilon \frac{L^2}{\gamma_2}$; $B = -I\epsilon^{1/2} \frac{\sigma_2}{\gamma_2}$; $L = -B \frac{L_{12}}{I}$; $\tilde{F} = -\frac{AB}{2}$; $\sigma = \epsilon^{1/2} L_{13} \frac{\sigma_3}{\gamma_3}$. W_2 and W_3 are independent Wiener processes. Interestingly, the equation for the coarse-grained variables x_1 display a structure richer than that of the full triad system in Eq. (6). In addition to the original linear and quadratic interactions, the reduced equation includes new terms: an effective forcing \tilde{F} , a cubic nonlinearity, and both additive and multiplicative noise. The additive noise results from the linear interactions across fast modes, while the multiplicative noise reflects the advection of the slow mode by the fast modes [67]. Thus, Eq. (B2) demonstrates that multiplicative noise arises from theoretical considerations, rather than being introduced ad hoc, providing a firm basis for its use in reduced-order stochastic climate models. The scalar model above has served as a prototype in several contexts: it has been used to test the Fluctuation–Dissipation Theorem in climate dynamics [81, 114] as well as for inverse modeling of the leading principal component of a quasi-geostrophic model and the observed variability associated with the North Atlantic Oscillation (NAO), demonstrating its relevance for theoretical studies in climate dynamics.

We evaluate the model in Eq. (B2) as done in Section III, so to reproduce the stationary statistics of the

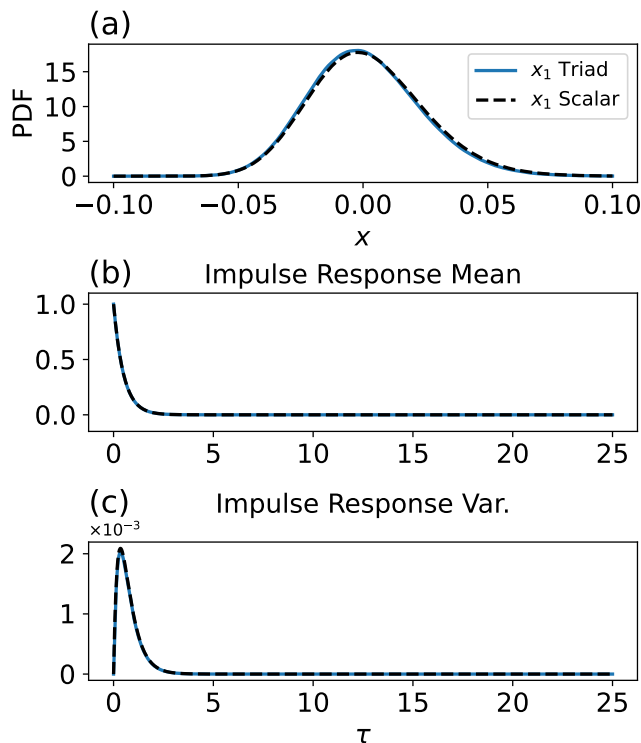


FIG. 9: In each panel: “ x_1 Triad” represent statistics of x_1 in the original triad model in Eq. (6); “ x_1 Scalar” represent statistics of x_1 in the scalar reduced model in Eq. (B2). Panel (a): stationary probability distribution. Panel (b): response in ensemble mean. Panel (c): response in ensemble variance. Impulse response functions are computed using an ensemble of $N_e = 10^7$ members.

slow variable x_1 as well as its response to perturbations as in the original triad system in Eq. (6). The results are reported in Figure 9. The analysis show that, given $\epsilon \ll 1$, it is possible to build a Markovian model of the slow variable x_1 reproducing both stationary and perturbed statistics as in the original system.

Finally, as shown in this Section, rigorous model reduction strategies such as those developed by Majda and collaborators [61] and by Roberts [134, 135] (among others [2]) offer invaluable theoretical guidelines for multiscale climate modeling. While such strategies were traditionally developed in the case when the equation of motions are known, they can possibly serve as inspiration and leading to new directions in future work involving data-driven emulators.

Finally, as shown in this Section, rigorous model reduction frameworks, such as those developed by Majda and collaborators [61] and by Roberts [134, 135], among others [2], provide invaluable theoretical guidance for multiscale climate modeling. While these strategies were

traditionally developed for systems with known equations of motion, they may also inspire future work aimed at incorporating such principles into data-driven-only emulators.

Appendix C: Technical and practical details on the model formulations

1. Multivariate data-driven stochastic models

Consider a N -dimensional dynamical system described by a stochastic differential equation $d\mathbf{x} = \mathbf{f}(\mathbf{x})dt + \Sigma(\mathbf{x})d\mathbf{W}$. This equation can be discretized by the forward Euler method as follows:

$$\Delta \mathbf{x} = \mathbf{x}(t + \Delta t) - \mathbf{x}(t) = \mathbf{f}(\mathbf{x}(t))\Delta t + \Sigma(\mathbf{x})\sqrt{\Delta t}\boldsymbol{\xi}(t) \quad (\text{C1})$$

where $\boldsymbol{\xi}(t)$ is a Gaussian white noise with zero mean, unit variance, and $\sqrt{\Delta t}\boldsymbol{\xi}(t)$ is the increment of the Wiener process $\Delta \mathbf{W} = \mathbf{W}(t + \Delta t) - \mathbf{W}(t)$. Without loss of generality, we rescale time units by the time sampling interval such that a non-dimensional time increment is $\Delta t = 1$ [6–8, 136]. The strategy is then to fit a rescaled version of Eq. (C1) from observational data alone. Such rescaled equation takes the following form:

$$\Delta \mathbf{x} = \mathbf{x}(t + 1) - \mathbf{x}(t) = \mathbf{f}(\mathbf{x}(t)) + \Sigma(\mathbf{x})\boldsymbol{\xi}(t). \quad (\text{C2})$$

We proceed in two steps:

- i. *Fitting the drift.* We compute $\Delta \mathbf{x} = \mathbf{x}(t + 1) - \mathbf{x}(t)$ and fit the deterministic dynamics such that $\Delta \mathbf{x} \approx \mathbf{f}(\mathbf{x}(t))$. In the main paper, we considered two cases:
 - *Linear drift.* In this case, given a trajectory $\mathbf{x}(t) \in \mathbb{R}^N$, we need to fit a matrix $\mathbf{L} \in \mathbb{R}^{N,N}$ such that $\Delta \mathbf{x} \approx \mathbf{L}\mathbf{x}(t)$ as close as possible. In practice, this is solved as a linear regression problem by minimizing the mean squared error. We use the linear regression module from the scikit-learn library [137].
 - *Nonlinear drift.* We consider the following form: $\Delta \mathbf{x} \approx \mathbf{f}(\mathbf{x}(t)) = \mathbf{L}\mathbf{x}(t) + \mathbf{n}(\mathbf{x}(t))$, where $\mathbf{L} \in \mathbb{R}^{N,N}$ is the linear operator and $\mathbf{n}(\mathbf{x}(t))$ is the nonlinear operator parameterized by a multilayer perceptron (MLP). Both operators are fitted jointly by minimizing the mean squared error using a version of the gradient descent algorithm (Adam, [138]) with weight decay. The MLP considered here always consisted of one hidden layer. The number of neurons in the hidden layer depended on the application: we considered 30 neurons in the experiments with the triad model in

Section III B 1 and 1000 neurons in the real-world application in Section IV. We played with more hidden layers but found a comparable performance, and sometimes a larger network also led to instabilities. The activation function used is the swish function (SiLU), which we found yields smoother responses to external perturbations. In contrast, the commonly used ReLU activation produced noisier responses. Furthermore, to ensure high accuracy in perturbation-response experiments, all data were processed using double-precision floating-point format.

ii. *Fitting the stochastic term.* Having fitted the deterministic dynamics \mathbf{f} , we compute the residuals $\mathbf{r}(t) \in \mathbb{R}^N$ as $\mathbf{r}(t) = \Delta \mathbf{x} - \mathbf{f}(\mathbf{x}(t))$. We then construct a suitable stochastic parametrization for this residual term. In the paper, we focus on two cases: additive and multiplicative noise.

- *Additive noise.* Given the residuals $\mathbf{r}(t)$, we proceed by computing their covariance matrix $\mathbf{C} \in \mathbb{R}^{N,N}$ as $\mathbf{C} = \langle \mathbf{r}\mathbf{r}^T \rangle$, where brackets denote time averaging. We then consider the Cholesky decomposition of \mathbf{C} to derive a lower triangular matrix $\mathbf{\Sigma} \in \mathbb{R}^{N,N}$ such that $\mathbf{C} = \mathbf{\Sigma}\mathbf{\Sigma}^T$. The full fitted equation solved by the emulator can then be written as:

$$\mathbf{x}(t+1) = \mathbf{x}(t) + \mathbf{f}(\mathbf{x}(t)) + \mathbf{\Sigma}\boldsymbol{\xi}(t) \quad (\text{C3})$$

and we remind the reader that $\boldsymbol{\xi}(t) \in \mathbb{R}^N$ is a Gaussian white noise with zero mean, unit variance.

- *Multiplicative noise.* Here, we consider state-dependent noise. To approximate it in a computationally efficient manner, we proceed as follows:
 - Given the residuals $\mathbf{r}(t)$ at each time t , we compute their outer product $\mathbf{C}(t) = \mathbf{r}(t)\mathbf{r}(t)^T$ which is a matrix of rank one.
 - We train a neural network predicting a lower triangular matrix $\mathbf{\Sigma}(\mathbf{x}(t))$ with positive diagonal, which can be interpreted as a Cholesky factor, such that $\mathbf{C}(t) \approx \mathbf{\Sigma}(\mathbf{x}(t))\mathbf{\Sigma}(\mathbf{x}(t))^T$ as close as possible.

In practice, the loss function minimizes the mean squared error (MSE) between $\mathbf{C}(t)$ and $\mathbf{\Sigma}(\mathbf{x}(t))\mathbf{\Sigma}(\mathbf{x}(t))^T$ at each batch. A minimizer of the MSE loss approximates the conditional mathematical expectation $\mathbb{E}[\mathbf{C}(t)|\mathbf{x}(t)]$, that is the covariance matrix averaged over all residuals corresponding to the same state vector, as a function of this state vector, and can be seen as a generalization of a method presented in [139] to multiple dimensions. The neural network architecture used here

is identical to the one used for fitting the drift. The positivity of the diagonal terms of the lower triangular matrix $\mathbf{\Sigma}(\mathbf{x}(t))$ is enforced through a softplus activation function. Note that this (high-dimensional) multiplicative noise parametrization is only applied in the real-world-like case, where data are scarce: to prevent overfitting, we use early stopping during training, halting after only 5 epochs. The final fitted equation solved by the emulator is:

$$\mathbf{x}(t+1) = \mathbf{x}(t) + \mathbf{f}(\mathbf{x}(t)) + \mathbf{\Sigma}(\mathbf{x}(t))\boldsymbol{\xi}(t) \quad (\text{C4})$$

where again $\boldsymbol{\xi}(t) \in \mathbb{R}^N$ is a Gaussian white noise with zero mean, unit variance.

Furthermore, even in the real-world case of sea surface temperature fields and radiative fluxes, reducing the dimensionality to a few, $N = 21$, components led to a simplified computational problem where all neural networks could be trained on CPUs and on a personal computer.

2. Scalar data-driven stochastic models

Consider a trajectory of length T of a 1-dimensional dynamical system. As in the Section above, we assume that this scalar time series can be modeled as a discrete stochastic process with time-stepping $\Delta t = 1$, therefore rescaling our time-stepping by the sampling interval. The scalar equation we aim to fit is therefore:

$$\Delta x = x(t+1) - x(t) = f(x(t)) + \sigma(x)\xi(t). \quad (\text{C5})$$

The training of the deterministic (i.e. drift) dynamics follows exactly the same procedure of the multivariate case. Even the network considered are the same, with one hidden layer and 30 neurons. So we refer the reader to the Section above regarding the fitting of the deterministic dynamics and proceed in focusing on the stochastic case.

Fitting the stochastic term.

- *Additive noise.* We compute the residual time series $r(t) = \Delta x - f(x(t))$ from the drift term. We then proceed in computing the standard deviation σ of such residual time series. The full fitted equation solved by the emulator can then be written as:

$$x(t+1) = x(t) + f(x(t)) + \sigma\xi(t) \quad (\text{C6})$$

and we remind the reader that $\xi(t)$ is a scalar Gaussian white noise with zero mean, unit variance.

- *Multiplicative noise.* We again consider the residual time series $r(t)$ from the drift term. We then compute at each time step t the square of the residual

at that time step, i.e. $r(t)^2$. We then train a neural network to have $g(x(t)) \approx r(t)^2$ by minimizing the mean squared error [139]. The neural network is again a MLP with one hidden layer with 30 neurons. Differently, from the neural networks considered for the drift, here we added a softplus activation function after the last layer of the network to ensure that the variance estimates are nonnegative. The final fitted equation solved by the emulator is:

$$x(t+1) = x(t) + f(x(t)) + \sqrt{g(x(t))}\xi(t). \quad (\text{C7})$$

ACKNOWLEDGMENTS

Most of the ideas discussed in this work stem from collaborations and exchanges with colleagues and friends. I am grateful for the supportive and engaging environment of the Zanna Group at Courant, as well as for interactions within the broader M²Lines project. I thank Laure Zanna and Carlos Fernandez-Granda for their feedback during early stages of the project. I am especially grateful to Pasha Perezhogin, Rory Basinski, Chris Pedersen, and Andre Souza for their thoughtful feedback and for many enriching discussions on data-driven modeling of the Climate system. I acknowledge an interesting email exchange with Prof. Tony Roberts, who drew my attention to recent advances on stochastic model reduction. This work was supported in part through the NYU IT High Performance Computing resources, services, and staff expertise.

-
- [1] M. Ghil and V. Lucarini, The physics of climate variability and climate change, *Rev. Mod. Phys.* **92**, 035002 (2020).
 - [2] V. Lucarini and M. Chekroun, Theoretical tools for understanding the climate crisis from Hasselmann’s programme and beyond, *Nat Rev Phys* (2023) (2023).
 - [3] C. Penland, Random Forcing and Forecasting Using Principal Oscillation Pattern Analysis, *Monthly Weather Review* **117**, 2165 (1989).
 - [4] C. Penland and P. Sardeshmukh, The optimal growth of tropical sea surface temperature anomalies, *Journal of Climate* **8**, 1999–2024 (1995).
 - [5] C. Penland, A stochastic model of indopacific sea surface temperature anomalies, *Physica D: Nonlinear Phenomena* **98**, 534 (1996), *nonlinear Phenomena in Ocean Dynamics*.
 - [6] S. Kravtsov, D. Kondrashov, and M. Ghil, Multilevel Regression Modeling of Nonlinear Processes: Derivation and Applications to Climatic Variability, *Journal of Climate* **18**, 4404–4424 (2005).
 - [7] D. Kondrashov, M. Chekroun, and M. Ghil, Data-driven non-markovian closure models, *Physica D: Nonlinear Phenomena* **297**, 33 (2015).
 - [8] K. Strounine, S. Kravtsov, D. Kondrashov, and M. Ghil, Reduced models of atmospheric low-frequency variability: Parameter estimation and comparative performance, *Physica D: Nonlinear Phenomena* **239**, 145 (2010).
 - [9] N. Agarwal, D. Kondrashov, P. Dueben, E. Ryzhov, and P. Berloff, A comparison of data-driven approaches to build low-dimensional ocean models, *Journal of Advances in Modeling Earth Systems* **13**, e2021MS002537 (2005).
 - [10] A. J. Majda and Y. Yuan, Fundamental limitations of ad hoc linear and quadratic multi-level regression models for physical systems, *Discrete and Continuous Dynamical Systems - Series B* **17**, 10.3934/dcdsb.2012.17.1333 (2012).
 - [11] A. Majda and J. Harlim, Physics constrained nonlinear regression models for time series, *NONLINEARITY* **26**, 201–217 (2013).
 - [12] A. Souza, Representing turbulent statistics with partitions of state space. part 1. theory and methodology., *J. Fluid Mech.* **997** (2024).
 - [13] A. Souza, Representing turbulent statistics with partitions of state space. part 2. the compressible euler equations., *J. Fluid Mech.* **997** (2024).
 - [14] L. T. Giorgini, A. N. Souza, and P. J. Schmid, Reduced markovian models of dynamical systems, *Physica D: Nonlinear Phenomena* **470**, 134393 (2024).
 - [15] L. Giorgini, Data-Driven Decomposition of Conservative and Non-Conservative Dynamics in Multiscale Systems, *Arxiv* <https://doi.org/10.48550/arXiv.2505.01895> (2025).
 - [16] A. Majda and D. Qi, Strategies for Reduced-Order Models for Predicting the Statistical Responses and Uncertainty Quantification in Complex Turbulent Dynamical Systems, *SIAM REVIEW* **60**, <https://doi.org/10.1137/16M1104664> (2018).
 - [17] M. Baldovin, F. Cecconi, and A. Vulpiani, Understanding causation via correlations and linear response theory, *Physical Review Research* **2**, 043436 (2020).
 - [18] F. Falasca, P. Perezhogin, and L. Zanna, Data-driven dimensionality reduction and causal inference for spatiotemporal climate fields, *Phys. Rev. E* **109**, 044202 (2024).
 - [19] J. Pathak, S. Subramanian, P. Harrington, S. Raja, A. Chattopadhyay, M. Mardani, T. Kurth, D. Hall, Z. Li, K. Azzadenesheli, P. Hassanzadeh, K. Kashinath, and A. Anandkumar, FourCastNet: A Global Data-driven High-resolution Weather Model using Adaptive Fourier Neural Operators, *arXiv e-prints* [10.48550/arXiv.2202.11214](https://arxiv.org/abs/2202.11214) (2022), [2202.11214](https://arxiv.org/abs/2202.11214) [physics.ao-ph].
 - [20] I. Price, A. Sanchez-Gonzalez, F. Alet, and et al., Probabilistic weather forecasting with machine learning, *Nature* **637**, 84–90 (2025).
 - [21] R. Lam, A. Sanchez-Gonzalez, M. Willson, P. Wirnsberger, M. Fortunato, F. Alet, S. Ravuri, T. Ewalds, Z. Eaton-Rosen, W. Hu, A. Merose, S. Hoyer, G. Hol-

- land, O. Vinyals, J. Stott, A. Pritzel, S. Mohamed, and P. Battaglia, Learning skillful medium-range global weather forecasting, *Science* **382**, 1416 (2023), <https://www.science.org/doi/pdf/10.1126/science.adi2336>.
- [22] K. Bi, L. Xie, H. Zhang, X. Chen, X. Gu, and Q. Tian, Accurate medium-range global weather forecasting with 3d neural networks, *Nature* **619**, 533–538 (2023).
- [23] B. Bonev and et al., FourCastNet 3: A geometric approach to probabilistic machine-learning weather forecasting at scale, *arXiv e-prints* 10.48550/arXiv.2507.12144 (2025).
- [24] D. Kochkov, J. Yuval, I. Langmore, P. Norgaard, J. Smith, G. Mooers, M. Klöwer, J. Lottes, S. Rasp, P. Düben, S. Hatfield, P. Battaglia, A. Sanchez-Gonzalez, M. Willson, M. P. Brenner, and S. Hoyer, Neural general circulation models for weather and climate, *Nature* **632**, 1060–1066 (2024).
- [25] O. Watt-Meyer, G. Dresdner, J. McGibbon, S. K. Clark, B. Henn, J. Duncan, N. D. Brenowitz, K. Kashinath, M. S. Pritchard, B. Bonev, M. E. Peters, and C. S. Bretherton, ACE: A fast, skillful learned global atmospheric model for climate prediction, *arXiv e-prints*, [arXiv:2310.02074](https://arxiv.org/abs/2310.02074) (2023), [arXiv:2310.02074](https://arxiv.org/abs/2310.02074) [physics.aoph].
- [26] O. Watt-Meyer, B. Henn, J. McGibbon, S. K. Clark, A. Kwa, W. A. Perkins, and C. S. Bretherton, ACE2: Accurately learning subseasonal to decadal atmospheric variability and forced responses, *arXiv e-prints* <https://arxiv.org/abs/2411.11268> (2024).
- [27] H. Guan, T. Arcomano, A. Chattopadhyay, and R. Maulik, LUCIE: A Lightweight Uncoupled Climate Emulator with long-term stability and physical consistency for O(1000)-member ensembles, *arXiv* <https://doi.org/10.48550/arXiv.2405.16297> (2025).
- [28] A. Chattopadhyay, M. Gray, T. Wu, and et al., Oceanet: a principled neural operator-based digital twin for regional oceans, *Sci. Rep.* **14**, 21181 (2024).
- [29] S. Bire, B. Lütjens, K. Azizzadenesheli, A. Anandkumar, and C. Hill, Ocean emulation with Fourier neural operators: Double gyre, *Journal of Advances in Modeling Earth Systems* **17** (2025).
- [30] S. Dheeshjith, A. Subel, A. Adcroft, J. Busecke, C. Fernandez-Granda, S. Gupta, and L. Zanna, Samudra: An AI global ocean emulator for climate., *Geophysical Research Letters* **52**, e2024GL114318 (2025).
- [31] W. Chapman, J. Schreck, Y. Sha, D. Gagne II, D. Kimpara, L. Zanna, K. Mayer, and J. Berner, CAMulator: Fast Emulation of the Community Atmosphere Model, *Arxiv* <https://doi.org/10.48550/arXiv.2504.06007> (2025).
- [32] H. Guan, T. Arcomano, A. Chattopadhyay, and R. Maulik, LUCIE-3D: A three-dimensional climate emulator for forced responses, *Arxiv* <https://doi.org/10.48550/arXiv.2509.02061> (2025).
- [33] J. Duncan and et al., SamudrACE: Fast and Accurate Coupled Climate Modeling with 3D Ocean and Atmosphere Emulators, *Arxiv* <https://doi.org/10.48550/arXiv.2509.12490> (2025).
- [34] C. Pedersen, L. Zanna, and J. Bruna, Thermalizer: Stable autoregressive neural emulation of spatiotemporal chaos, *Arxiv* <https://doi.org/10.48550/arXiv.2503.18731> (2025).
- [35] R. Jiang, X. Zhang, K. Jakhar, P. Lu, P. Hassanzadeh, M. Maire, and R. Willett, Hierarchical Implicit Neural Emulators, *Arxiv* <https://doi.org/10.48550/arXiv.2506.04528> (2025).
- [36] Y. Sun, P. Hassanzadeh, M. Zand, and D. Abbot, Can ai weather models predict out-of-distribution gray swan tropical cyclones?, *Proceedings of the National Academy of Sciences* **122**, e2420914122 (2025).
- [37] S. Van Loon, M. Rugenstein, and E. A. Barnes, Reanalysis-based Global Radiative Response to Sea Surface Temperature Patterns: Evaluating the Ai2 Climate Emulator, *Geophysical Research Letters* **52**, e2025GL115432 (2025).
- [38] J. Bloch-Johnson, M. A. A. Rugenstein, M. J. Alessi, C. Proistosescu, M. Zhao, B. Zhang, A. I. L. Williams, J. M. Gregory, J. Cole, Y. Dong, M. L. Duffy, S. M. Kang, and C. Zhou, The green’s function model inter-comparison project (gfmip) protocol, *Journal of Advances in Modeling Earth Systems* **16**, e2023MS003700 (2024), e2023MS003700 2023MS003700, <https://agupubs.onlinelibrary.wiley.com/doi/pdf/10.1029/2023MS003700>.
- [39] Y. Dong, C. Proistosescu, K. C. Armour, and D. S. Battisti, Attributing Historical and Future Evolution of Radiative Feedbacks to Regional Warming Patterns using a Green’s Function Approach: The Preeminence of the Western Pacific, *Journal of Climate* **32**, 5471 (2019).
- [40] H. Hersbach, B. Bell, P. Berrisford, S. Hirahara, A. Horányi, J. Muñoz-Sabater, and et al., The ERA5 global reanalysis, *Quarterly Journal of the Royal Meteorological Society* **146**, 1999–2049 (2020).
- [41] B. Zhang and T. Merlis, The Equilibrium Response of Atmospheric Machine-Learning Models to Uniform Sea Surface Temperature Warming, *Arxiv* <https://doi.org/10.48550/arXiv.2510.02415> (2025).
- [42] E. Wu, F. Rebassoo, P. Paul, C. Proistosescu, J. Nugent, D. McCoy, and et al., Applying the ACE2 emulator to SST green’s functions for the E3SMv3 global atmosphere model, *Journal of Geophysical Research: Machine Learning and Computation* **2**, e2025JH000774 (2025).
- [43] F. Cecconi, M. Cencini, M. Falcioni, and A. Vulpiani, Predicting the future from the past: An old problem from a modern perspective, *Am. J. Phys.* **11**, 1001–1008 (2012).
- [44] H. Hosni and A. Vulpiani, Forecasting in Light of Big Data, *Philos. Technol.* **31**, 557–569 (2018).
- [45] M. Baldovin, F. Cecconi, M. Cencini, A. Puglisi, and A. Vulpiani, The role of data in model building and prediction: A survey through examples, *Phys. Rev. Res.* **20**, doi:10.3390/e20100807 (2018).
- [46] A. Majda, C. Franzke, and D. Crommelin, Normal forms for reduced stochastic climate models, *Proc. Natl. Acad. Sci.* **10**, 3649–3653 (2010).
- [47] A. Majda, B. Gershgorin, and Y. Yuan, Low-Frequency Climate Response and Fluctuation–Dissipation Theorems: Theory and Practice, *Journal of the Atmospheric Sciences* **67**, 1186–1201 (2010).
- [48] A. J. Majda, R. V. Abramov, and M. J. Grote, *Information Theory and Stochastics for Multiscale Nonlinear Systems* (CRM Monograph Series, American Mathematical Society, 2005).
- [49] U. Marconi, A. Puglisi, L. Rondoni, and A. Vulpiani, Fluctuation-dissipation: Response theory in statistical physics, *Phys. Rep.* **461** (2008).
- [50] G. L. and A. Vulpiani, Prediction and Inference: From Models and Data to Artificial Intelligence, Founda-

- tions of Physics **54**, <https://doi.org/10.1007/s10701-024-00803-4> (2024).
- [51] A. Dalmedico, History and Epistemology of Models: Meteorology (1946–1963) as a Case Study., *Archive for History of Exact Science* **55**, 395–422 (2001).
- [52] L. A. Smith, What might we learn from climate forecasts?, *Proceedings of the National Academy of Sciences* **99**, 2487 (2002), <https://www.pnas.org/doi/pdf/10.1073/pnas.012580599>.
- [53] J. G. Charney, ON A PHYSICAL BASIS FOR NUMERICAL PREDICTION OF LARGE-SCALE MOTIONS IN THE ATMOSPHERE , *Journal of Meteorology* **6**, 372–385 (1949).
- [54] J. G. Charney, R. Fjörtoft, and J. Von Neumann, Numerical Integration of the Barotropic Vorticity Equation, *Tellus* **2** (1950).
- [55] B. Dubrulle, F. Daviaud, D. Faranda, L. Marié, and B. Saint-Michel, How many modes are needed to predict climate bifurcations? Lessons from an experiment, *Nonlin. Processes Geophys.* **29**, 17–35 (2022).
- [56] J. Wouters and V. Lucarini, Cluster-based reduced-order modelling of a mixing layer, *Journal of Statistical Mechanics: Theory and Experiment* **03**, P03003 (2012).
- [57] G. Vissio and V. Lucarini, A proof of concept for scale-adaptive parametrizations: the case of the lorenz '96 model, *Quarterly Journal of the Royal Meteorological Society* **144**, 63 (2018 Part A).
- [58] K. Hasselmann, Stochastic climate models part i. theory., *Tellus* **28**, 473 (1976).
- [59] N. Chen and H. Liu, Minimum reduced-order models via causal inference, *Nonlinear Dyn* **113**, 11327–11351 (2025).
- [60] A. J. Majda, I. Timofeyev, and Vanden-Eijnden, Models for stochastic climate prediction, *Proc. Natl. Acad. Sci. USA* **96**, 14687–14691 (1999).
- [61] A. J. Majda, I. Timofeyev, and Vanden-Eijnden, A mathematical framework for stochastic climate models, *Proc. Natl. Acad. Sci. USA* **54**, 891–974 (2001).
- [62] A. J. Majda, I. Timofeyev, and Vanden-Eijnden, A priori test of a stochastic mode reduction strategy, *Physica D* **170**, 206–252 (2002).
- [63] A. J. Majda, I. Timofeyev, and Vanden-Eijnden, Systematic strategies for stochastic mode reduction in climate, *J. Atmos. Sci.* **60**, 1705–1722 (2003).
- [64] T. J. O’Kane, D. Harries, and M. A. Collier, Bayesian structure learning for climate model evaluation, *Journal of Advances in Modeling Earth Systems* **16**, e2023MS004034 (2024).
- [65] J. Donges, Y. Zou, N. Marwan, and et al., Complex networks in climate dynamics, *Eur. Phys. J. Spec. Top.* **174**, 157–179 (2009).
- [66] I. Fountalis, C. Dovrolis, A. Bracco, B. Dilkina, and S. Keilholz, δ -MAPS from spatio-temporal data to a weighted and lagged network between functional domain, *Appl. Netw. Sci.* **3**, 21 (2018).
- [67] A. Majda, C. Franzke, and K. Boualem, An applied mathematics perspective on stochastic modelling for climate, *Phil. Trans. R. Soc. A.* **366**, 2427–2453 (2008).
- [68] D. Crommelin and A. Majda, Strategies for Model Reduction: Comparing Different Optimal Bases, *Journal of the Atmospheric Sciences* **61**, 2206–2217 (2004).
- [69] H. Fan, B. Fei, P. Gentine, Y. Xiao, K. Chen, Y. Liu, Y. Qu, F. Ling, and L. Bai, Physically Consistent Global Atmospheric Data Assimilation with Machine Learning in a Latent Space, *Arxiv* <https://doi.org/10.48550/arXiv.2502.02884> (2025).
- [70] N. Lutsko, I. Held, and P. Zurita-Gotor, Applying the Fluctuation–Dissipation Theorem to a Two-Layer Model of Quasigeostrophic Turbulence , *Journal of the Atmospheric Sciences* **72**, 3161–3177 (2015).
- [71] P. Hassanzadeh and Z. Kuang, The linear response function of an idealized atmosphere. part ii: Implications for the practical use of the fluctuation–dissipation theorem and the role of operator’s nonnormality, *Journal of The Atmospheric Science* , 3441–3452 (2016).
- [72] C. Penland, M. D. Fowler, D. L. Jackson, and R. Cifelli, Forecasts of opportunity for northern california soil moisture, *Land* **10**, 10.3390/land10070713 (2021).
- [73] Y. Zhao and A. Capotondi, The role of the tropical Atlantic in tropical Pacific climate variability, *npj Clim Atmos Sci* **7** (2024).
- [74] J. Lien, Y.-N. Kuo, H. Ando, and S. Kido, Colored linear inverse model: A data-driven method for studying dynamical systems with temporally correlated stochasticity, *Phys. Rev. Res.* **7**, 023042 (2025).
- [75] D. Kondrashov, S. Kratsov, A. Robertson, and M. Ghil, A hierarchy of data-based enso models, *Journal of Climate* **18**, 4425–4444 (2005).
- [76] H. Risken, *The Fokker-Planck Equation – Methods of Solution and Applications* (Springer-Verlag, 1996).
- [77] J. Ismael, Reflections on the asymmetry of causation, *Interface Focus* **12**, 20220081 (2023).
- [78] E. Aurell and G. Del Ferraro, Causal analysis, correlation- response, and dynamic cavity, *J. of Phys.: Conference Series* **699**, 012002 (2016).
- [79] V. Lucarini, Revising and Extending the Linear Response Theory for Statistical Mechanical Systems: Evaluating Observables as Predictors and Predictands, *J Stat Phys* **173**, 1698–1721 (2018).
- [80] V. Lucarini and M. D. Chekroun, Detecting and attributing change in climate and complex systems: Foundations, green’s functions, and nonlinear fingerprints, *Phys. Rev. Lett.* **133**, 244201 (2024).
- [81] A. Majda, R. Abramov, and B. Gershgorin, High skill in low-frequency climate response through fluctuation dissipation theorems despite structural instability, *Proc. Natl. Acad. Sci.* **107**, 581–586 (2010).
- [82] C. Franzke and A. Majda, Low-order stochastic mode reduction for a prototype atmospheric GCM, *Journal of the Atmospheric Sciences* **2**, 457–479 (2006).
- [83] J. Berner and G. Branstator, Linear and nonlinear signatures in the planetary wave dynamics of an agcm: Probability density functions, *Journal of the Atmospheric Sciences* **64**, 117–136 (2007).
- [84] P. Sura, M. Newman, C. Penland, and P. Sardeshmukh, Multiplicative noise and non-Gaussianity: A paradigm for atmospheric regimes?, *Journal of Climate* **62**, 1391–1409 (2005).
- [85] G. Lacorata and A. Vulpiani, Fluctuation-response relation and modeling in systems with fast and slow dynamics, *Nonlin. Processes Geophys.* **14**, 681–694 (2007).
- [86] M. Baldovin, A. Puglisi, and A. Vulpiani, Langevin equations from experimental data: The case of rotational diffusion in granular media, *PLoS ONE* **14(2)**, e0212135 (2019).
- [87] H. Arnold, I. Moroz, and T. Palmer, Stochastic parametrizations and model uncertainty in the lorenz’ 96 system, *Phil Trans R Soc* **371**, 20110479 (2013).

- [88] A. Dawson and T. Palmer, Simulating weather regimes: impact of model resolution and stochastic parameterization, *Clim Dyn* **44**, 2177 (2015).
- [89] J. Berner and et al., Stochastic Parameterization: Toward a New View of Weather and Climate Models, *Bulletin of the American Meteorological Society* **98**, 565–588 (2017).
- [90] Even moderately more complex systems already expose the practical limitations of rigorous stochastic mode reduction procedures; see Strouine et al. (2008) in the context of quasi-geostrophic modeling [8].
- [91] F. Cecconi, G. Costantini, C. Guardiani, M. Baldovin, and A. Vulpiani, Correlation, response and entropy approaches to allosteric behaviors: a critical comparison on the ubiquitin case, *Physical Biology* **5**, 056002 (2020).
- [92] T. Palmer, Stochastic weather and climate models, *Nat. Rev. Phys.* **1**, 463–471 (2019).
- [93] J. Berner and et al., Stochastic parameterization: Toward a new view of weather and climate models, *Bulletin of the American Meteorological Society* **98**, 565 (2017).
- [94] B. Meyssignac, R. Guillaume-Castel, and R. Roca, Revisiting the Global Energy Budget Dynamics with a Multivariate Earth Energy Balance Model to Account for the Warming Pattern Effect, *Journal of Climate* **36**, 8113–8126 (2023).
- [95] J. J. Barsugli and P. D. Sardeshmukh, Global atmospheric sensitivity to tropical sst anomalies throughout the indo-pacific basin, *Journal of Climate* **15**, 3427 (2002).
- [96] C. Zhou, M. D. Zelinka, and S. A. Klein, Analyzing the dependence of global cloud feedback on the spatial pattern of sea surface temperature change with a green’s function approach, *Journal of Advances in Modeling Earth Systems* **9**, 2174 (2017), <https://agupubs.onlinelibrary.wiley.com/doi/pdf/10.1002/2017MS003996>
- [97] B. Zhang, M. Zhao, and Z. Tan, Using a Green’s Function Approach to Diagnose the Pattern Effect in GFDL AM4 and CM4, *Journal of Climate* **36**, 1105 (2023).
- [98] Y. Dong, K. C. Armour, M. D. Zelinka, C. Proistosescu, D. S. Battisti, C. Zhou, and T. Andrews, Intermodel Spread in the Pattern Effect and Its Contribution to Climate Sensitivity in CMIP5 and CMIP6 Models, *Journal of Climate* **33**, 7755 (2020).
- [99] M. J. Alessi and M. A. Rugenstein, Surface temperature pattern scenarios suggest higher warming rates than current projections, *Geophysical Research Letters* **50**, e2023GL105795 (2023).
- [100] A. I. Williams, N. Jeevanjee, and J. Bloch-Johnson, Cirrus tents, convective thresholds, and the non-linear climate response to tropical ssts, *Geophysical Research Letters* **50**, e2022GL101499 (2023).
- [101] I. Held, The Gap between Simulation and Understanding in Climate Modeling, *Bulletin of the American Meteorological Society*, 1609–1614 (2005).
- [102] F. Falasca, A. Basinski, L. Zanna, and M. Zhao, A fluctuation-dissipation theorem perspective on radiative responses to temperature perturbations, *Journal of Climate* **38**, 3239–3260 (2025).
- [103] I. M. Held, H. Guo, A. Adcroft, J. P. Dunne, L. W. Horowitz, J. Krasting, and et al., Structure and performance of GFDL’s CM4.0 climate model, *Journal of Advances in Modeling Earth Systems* **11**, 3691–3727 (2019).
- [104] A. Adcroft, W. Anderson, V. Balaji, C. Blanton, M. Bushuk, C. O. Dufour, and et al., The GFDL global ocean and sea ice model OM4.0: Model description and simulation features, *Journal of Advances in Modeling Earth Systems* **11**, 3167–3211 (2019).
- [105] M. Zhao and Coauthors, The GFDL global atmosphere and land model AM4.0/LM4.0: 1. Simulation characteristics with prescribed SSTs., *Journal of Advances in Modeling Earth Systems* **10**, 691–734 (2018).
- [106] M. Zhao and Coauthors, The GFDL global atmosphere and land model am4.0/LM4.0: 2. Model description, sensitivity studies, and tuning strategies., *Journal of Advances in Modeling Earth Systems* **10**, 735–769 (2018).
- [107] R. T. Pierrehumbert, *Principles of Planetary Climate* (Cambridge University Press, 2010).
- [108] D. M. Romps, J. T. Seeley, and J. P. Edman, Why the forcing from carbon dioxide scales as the logarithm of its concentration, *Journal of Climate* **35**, 4027–4047 (2022).
- [109] M. Zhao, An investigation of the effective climate sensitivity in GFDL’s new climate models CM4.0 and SPEAR, *Journal of Climate* **35**, 5637–5660 (2022).
- [110] A. Timmermann and et al., El Niño-Southern Oscillation complexity, *Nature* **559**, 535 (2018).
- [111] S. M. Kang, P. Ceppi, Y. Yu, and I.-S. Kang, Recent global climate feedback controlled by southern ocean cooling, *Nature Geoscience* **16**, 775 (2023).
- [112] S. Van Loon, M. Rugenstein, and E. A. Barnes, Observation-based estimate of earth’s effective radiative forcing, *Proceedings of the National Academy of Sciences* **122**, e2425445122 (2025), <https://www.pnas.org/doi/pdf/10.1073/pnas.2425445122>.
- [113] E. Guilyardi, P. Braconnot, F.-F. Jin, S. T. Kim, M. Kolasinski, L. T., and I. Musat, Atmosphere Feedbacks during ENSO in a Coupled GCM with a Modified Atmospheric Convection Scheme, *Journal of Climate* **2**, 5698–5718 (2009).
- [114] T. Giorgini, F. Falasca, and A. Souza, Predicting Forced Responses of Probability Distributions via the Fluctuation-Dissipation Theorem and Generative Modeling, *Arxiv* (Currently in press in PNAS) <https://doi.org/10.48550/arXiv.2504.13333> (2025).
- [115] S. Lang and et al., AIFS – ECMWF’s data-driven forecasting system, *Arxiv* <https://doi.org/10.48550/arXiv.2406.01465> (2025).
- [116] B. Lütjens, R. Ferrari, D. Watson-Parris, and N. E. Selin, The impact of internal variability on benchmarking deep learning climate emulators, *Journal of Advances in Modeling Earth Systems* **17** (2025).
- [117] G. Geogdzhayev, A. N. Souza, G. R. Flierl, and R. Ferrari, An EOF-Based Emulator of Means and Covariances of Monthly Climate Fields, *EGU sphere* [preprint] (2025).
- [118] T. Palmer, A nonlinear dynamical perspective on model error: A proposal for non-local stochastic-dynamic parameterization in weather and climate prediction models, *Proceedings of the National Academy of Sciences* **127**, 279 (2001).
- [119] F. Alet and et al., Skillful joint probabilistic weather forecasting from marginals, *Arxiv* <https://doi.org/10.48550/arXiv.2506.10772> (2025).
- [120] E. Lorenz, Predictability: a problem partly solved, *Seminar on Predictability*, 4-8 September 1995 **1**, 1 (1995).

- [121] A. Gritsun and G. Branstator, Climate response using a three-dimensional operator based on the fluctuation–dissipation theorem, *Journal of The Atmospheric Science*, 2558–2575 (2007).
- [122] L. Onsager and S. Machlup, Fluctuations and irreversible processes, *Phys. Rev.* **91**, 1505 (1953).
- [123] D. Lucente, A. Baldassarri, A. Puglisi, A. Vulpiani, and M. Viale, Inference of time irreversibility from incomplete information: Linear systems and its pitfalls, *Phys. Rev. Res.* **4**, 043103 (2022).
- [124] V. Lucarini and M. D. Chekroun, Detecting and attributing change in climate and complex systems: Foundations, green’s functions, and nonlinear fingerprints, *Phys. Rev. Lett.* **133**, 244201 (2024).
- [125] M. J. Kusner, J. Loftus, C. Russell, and R. Silva, Counterfactual fairness, in *Advances in Neural Information Processing Systems*, Vol. 30, edited by I. Guyon, U. V. Luxburg, S. Bengio, H. Wallach, R. Fergus, S. Vishwanathan, and R. Garnett (Curran Associates, Inc., 2017).
- [126] J. Runge, V. Petoukhov, J. Donges, *et al.*, Identifying causal gateways and mediators in complex spatio-temporal systems, *Nat Commun* **6**, 8502 (2015).
- [127] N. Ay and D. Polani, Information flows in causal networks, *Adv. Complex Syst.* **11**, 17 (2008).
- [128] M. Falcioni and A. Vulpiani, The relevance of chaos for the linear response theory, *Physica A: Statistical Mechanics and its Applications* **215**, 481 (1995).
- [129] M. Falcioni, S. Isola, and A. Vulpiani, Correlation functions and relaxation properties in chaotic dynamics and statistical mechanics, *Physics Letters A* **144**, 341 (1990).
- [130] C. E. Leith, Climate response and fluctuation dissipation, *Journal of The Atmospheric Science* **32**, 2022–2026 (1975).
- [131] V. Lucarini, Interpretable and Equation-Free Response Theory for Complex Systems, Arxiv <https://doi.org/10.48550/arXiv.2502.07908> (2025).
- [132] E. Lorenz, Deterministic nonperiodic flow, *J. Atmospheric Sci.* **20**, 130–141 (1963).
- [133] J. Charney and J. DeVore, Multiple Flow Equilibria in the Atmosphere and Blocking, *Journal of the Atmospheric Sciences* **36**, 1205–1216 (1979).
- [134] A. J. Roberts, Resolving the multitude of microscale interactions accurately models stochastic partial differential equations, *LMS Journal of Computation and Mathematics* **9**, 193–221 (2006).
- [135] A. Roberts, Normal form transforms separate slow and fast modes in stochastic dynamical systems, *Physica A: Statistical Mechanics and its Applications* **387**, 12 (2008).
- [136] S. Kravtsov, M. Ghil, and D. Kondrashov, Empirical Model Reduction and the Modeling Hierarchy in Climate Dynamics and the Geosciences, in *Stochastic Physics and Climate Modeling*, edited by T. Palmer and P. Williams (Cambridge University Press, 2009) pp. 35–72.
- [137] F. Pedregosa, G. Varoquaux, A. Gramfort, V. Michel, B. Thirion, O. Grisel, M. Blondel, P. Prettenhofer, R. Weiss, V. Dubourg, J. Vanderplas, A. Passos, D. Cournapeau, M. Brucher, M. Perrot, and E. Duchesnay, Scikit-learn: Machine learning in Python, *Journal of Machine Learning Research* **12**, 2825 (2011).
- [138] D. P. Kingma and J. Ba, Adam: A method for stochastic optimization, arXiv preprint arXiv:1412.6980 (2014).
- [139] J. Adler and O. Öktem, Deep bayesian inversion, arXiv preprint arXiv:1811.05910 **1**, 7 (2018).